

Monitoring the Dusty S-Cluster Object (DSO/G2) on its Orbit towards the Galactic Center Black Hole

M. Valencia-S.¹, A. Eckart^{1,2}, M. Zajaček^{1,2,3}, F. Peissker¹, M. Parsa¹, N. Grosso⁴, E. Mossoux⁴, D. Porquet⁴, B. Jalali¹, V. Karas³, S. Yazici¹, B. Shahzamanian¹, N. Sabha¹, R. Saalfeld¹, S. Smajic¹, R. Grellmann¹, L. Moser¹, M. Horrobin¹, A. Borkar¹, M. García-Marín¹, M. Dovčiak³, D. Kunneriath³, G. D. Karssen¹, M. Bursa³, C. Straubmeier¹, and H. Bushouse⁵

ABSTRACT

We analyse and report in detail new near-infrared (1.45 - 2.45 microns) observations of the Dusty S-cluster Object (DSO/G2) during its approach to the black hole at the center of the Galaxy that were carried out with ESO VLT/SINFONI between February and September 2014. Before May 2014 we detect spatially compact Br γ and Pa α line emission from the DSO at about 40mas east of SgrA*. The velocity of the source, measured from the red-shifted emission, is 2700 ± 60 km/s. No blue-shifted emission above the noise level is detected at the position of SgrA* or upstream the presumed orbit. After May we find spatially compact Br γ blue-shifted line emission from the DSO at about 30mas west of SgrA* at a velocity of -3320 ± 60 km/s and no indication for significant red-shifted emission. We do not detect any significant extension of velocity gradient across the source. We find a Br γ -line full width at half maximum of 50 ± 10 Å before and 15 ± 10 Å after the peribothron transit, i.e. no significant line broadening with respect to last year is observed. Br γ line maps show that the bulk of the line emission originates from a region of less than 20 mas diameter. This is consistent with a very compact source on an elliptical orbit with a peribothron time passage in 2014.39 ± 0.14 . For the moment, the flaring activity of the black hole in the near-infrared regime has not shown any statistically significant increment. Increased accretion activity of SgrA* may still be upcoming. We discuss details of a source model according to which the DSO is rather a young accreting star than a coreless gas and dust cloud.

Subject headings: black hole physics — line: identification, profiles — techniques: imaging spectroscopy — astrometry — Galaxy: center

1. Introduction

Recently the Galactic center region has attracted a lot of attention due to the fact that a dusty object has been detected (Gillessen et al. 2012, 2013a; Eckart et al. 2013) that is approaching the central super massive black hole associated with the radio source SgrA*. Due to its

infrared excess and as indicated through nomenclature (G2) it has been speculated that the

¹I. Physikalisches Institut der Universität zu Köln, Zùlpicher Str. 77, D-50937 Köln, Germany; mvalencias@ph1.uni-koeln.de

²Max-Planck-Institut für Radioastronomie, Auf dem Hügel 69, D-53121 Bonn, Germany

³Astronomical Institute of the Academy of Sciences Prague, Boční II 1401/1a, CZ-141 31 Praha 4, Czech Republic

⁴Observatoire Astronomique de Strasbourg, Université de Strasbourg, CNRS, UMR 7550, 11 rue de l'Université, F-67000 Strasbourg, France

⁵Space Telescope Science Institute, Baltimore, MD 21218, USA

source consists to a dominant fraction of gas and dust (Gillessen et al. 2012, 2013a; Pfuhl et al. 2014). By now the object is expected to have passed through its peribothron and tidal disruption as well as intense accretion events have been predicted. Eckart et al. (2013) show a possible spectral decomposition of this source using the M-band measurement by Gillessen et al. (2012). Depending on the relative stellar and dust flux density contributions the M-band measurement is consistent with a dust temperature of 450 K and an integrated luminosity of up to $\sim 10 L_{\odot}$. This allows for a substantial stellar contribution in mass and reddened stellar luminosity. A stellar nature is also favored by many other authors (see also Murray-Clay & Loeb 2012; Scoville & Burkert 2013; Ballone et al. 2013; Phifer et al. 2013; Zajaček et al. 2014). We will therefore refer to it in the following as a Dusty S-cluster Object, DSO (Eckart et al. 2013). Hence, although the Br γ line emission may be dominated by optically thin emission, a contribution from more compact optically thick regions cannot be excluded. Also, it is uncertain how large the extinction towards the center of the gas cloud really is. Therefore, the total mass of the object is very uncertain but is presumably less than that of a typical member of the high velocity S-star cluster (i.e. $\lesssim 20 M_{\odot}$; Ghez et al. 2003; Eisenhauer et al. 2005; Martins et al. 2006). The compactness of the DSO is also supported by the recent L-band detection close to peribothron (Ghez et al. 2014; Witzel et al. 2014).

Gillessen et al. (2013a,b) and Pfuhl et al. (2014) report that the Br γ luminosity of the DSO has remained constant over the entire time range covered by spectroscopy from 2004 to 2013. Figs. 1 and 5 in Pfuhl et al. (2014) show that in their April 2014 data set the blue line emission is approximately as spatially compact as the red side and has a significantly stronger peak emission than the red line emission. Their derived integrated Br γ luminosities for the blue side is about 1.14 times brighter than the red side (section 3.2 in Pfuhl et al. 2014).

During the past year we have obtained a substantial, independent imaging spectroscopy data set using SINFONI at the ESO VLT. In addition we have re-reduced a large number of data sets available from the ESO archive and have used our

own and published positional data to re-estimate the orbit of the DSO. Here we present the results of this detailed investigation. The paper is organized in the following way: In sections 2 and 3 we present the observations and data reduction, including the analysis of the spectral line properties of the DSO. In section 4 we discuss the results including the orbit (section 4.1), the tidal interaction of the DSO with SgrA* (section 4.2) and the ambient medium (section 4.3), consequences for the flare activity (section 4.4), and the interpretation of the DSO as a possible pre-main sequence star (section 4.5). After discussing the origin and fate of the DSO in section 5 we summarize and conclude in section 6.

2. Observations and data reduction

Here we present the data sets we are using in the study of the DSO. The procedures for data reduction and data quality selection are also described. We report mainly on the observations¹ we conducted from February to September 2014. We use earlier archive data to discuss general properties like the DSO orbit.

2.1. The 2014 Data Set

We performed NIR integral field observations of the Galactic center using SINFONI at the VLT in Chile (Eisenhauer et al. 2003; Bonnet et al. 2004). The instrument is an image-slicer integral field unit fed by an adaptive optics (AO) module. The AO system uses an optical wavefront sensor that was locked on a bright star 15.54'' north and 8.85'' east of Sgr A*. We employed H+K grating that covers the 1.45 – 2.45 μm range with a spectral resolution of $R \sim 1500$ (i.e., approximately 200 km s^{-1} at 2.16 μm). The 0.8'' \times 0.8'' field of view was jittered around the position of the star S2, in such a way that the star remained within the upper half zone of the detector. This was done in order to avoid a region with possible non-linear behavior of the detector. Observations of different B- and G-type stars were taken to obtain independent telluric templates.

The Galactic center region was observed in intervals of 400 s or 600 s, followed or preceded by

¹ESO programs 092.B-0009 (PI: A. Eckart), 093.B-0092 (PI: A. Eckart) and 092.B-0920 (PI: N. Grosso)

time slots of equal length on a dark cloud 5'36" north and 12'45" west of Sgr A*. The integration time were chosen of that length in order to be able to also monitor the flux density of SgrA* for time intervals of typical flare lengths and to provide a higher flexibility in data selection to optimize the quality of the data. Although this observational strategy reduces the effective integration time on source to about a third when compared with parsed sky observations at a rate of about once per hour, it ensures a better control of the noise in the frames. Because of the variable weather conditions, the point-spread function (PSF) changed along the observing nights. The quality of individual exposures was judged based on the PSF at the moment of the observation, as measured from the shape of the stars in the field of view. For the analysis presented here, we have created two final data cubes, one from the combination of the best quality exposures, and another including also medium quality data, as described below. Table 1 shows the list of the observing dates, including the amount of exposures that fulfilled the selection criteria. Note that (both for pre- and post-peribothron) our observations are bracketing and preceding those presented by Pfuhl et al. (2014).

2.2. Calibration

In the data reduction process, we first followed the SINFONI reduction manually to correct for the bad lines created by the data processing at the detector level. We used the suggested IDL procedure, adjusting the identification threshold (2 times the background noise $\sigma_{background}$) whenever necessary. A first cosmic ray correction to the sky and target files was performed using the algorithm developed by Pych (2004). The random pattern introduced by some detector amplifiers was detected and removed in science and calibration files following the algorithms proposed by Smajić et al. (2014). Then we used the SINFONI pipeline for the standard reduction steps (like flat fielding and bad pixel corrections) and wavelength calibration. We obtained one data cube for each on-source exposure.

DPUSER routines (Thomas Ott, MPE Garching; see also Eckart & Duhoux 1991) were used to flag remaining bad pixels and cosmic rays on the plane of the slitlets in the detector (x - z , which cor-

responds to dec.-wavelength), in each data cube. The combined effects of the atmospheric refraction were appreciable as a spatial displacement of the stars by a couple of pixels when going from short to long wavelengths. Fixing the position of the center of a bright source at a particular wavelength and making a spatial sub-pixel shift at all other wavelengths could correct the problem, but the shape of the resulting spectrum in each pixel would depend on the interpolation algorithm. Therefore, to preserve the integrity of the spectrum in the narrow spectral regions where emission lines are present, the spatial image shift was done in steps of 0.045 μm .

A 2D Gaussian, fitted to the bright star S2, was taken as an indication of the PSF. Cubes where the FWHM of the fitted Gaussian is less than 83 mas (or 6.65 pixels) were categorized as best quality cubes, while those with FWHM values between 83 and 96 mas (or 7.65 pixels) were classified as medium quality cubes. The combination of the selected data cubes was done by averaging every spatial and spectral pixel after a proper alignment of the images. The combination of the 63 best quality cubes produced a final data cube with a total of 7.2 h on-source integration time. When including the 30 medium quality exposures, the resulting data cube covers a total of 10.8 h of integration time on-source. This second data cube was used to evaluate the effects of the data quality in the signal-to-noise of the measured quantities, and unless it is specifically mentioned in the text, all measurements and plots are derived from the higher quality data cube.

Flux calibration was done using aperture photometry on a deconvolved K -band image created from the final data cube. The deconvolution was performed using the Lucy-Richardson algorithm incorporated in DPUSER, while the PSF was estimated using the IDL based StarFinder routine (Diolaiti et al. 2000). We used as calibration stars S2 ($K_s = 14.1$), S4 ($K_s = 14.6$), S10 ($K_s = 14.1$), and S12 ($K_s = 15.2$), and adopted the K -band extinction correction $m_{AK} = 2.46$ of Schödel et al. (2010); (see also Witzel et al. 2012, for the flux estimation).

The NIR spectrum of the inner ~ 0.5 arcseconds around SgrA* is dominated by the stellar continuum of hundreds of stars fainter than $K_s = 18$ mag that are part of the central cluster,

TABLE 1
SUMMARY OF THE GALACTIC CENTER OBSERVATIONS

Date (YYYY.MM.DD)	Start time (UT)	End time (UT)	Number of on-source exposures			Exp. Time (s)
			Total	medium quality	high quality	
2014.02.28	08:34:58	09:54:37	7	0	0	400
2014.03.01	08:00:14	10:17:59	12	0	0	400
2014.03.02	07:49:06	08:18:54	3	0	0	400
2014.03.11	08:03:55	10:03:28	11	5	8	400
2014.03.12	07:44:35	10:07:45	13	5	9	400
2014.03.26	06:43:05	09:58:12	11	8	8	600
2014.03.27	06:32:50	10:04:12	18	1	7	400
2014.04.02	06:31:39	09:53:52	18	0	5	400
2014.04.03	06:20:46	09:45:02	18	14	17	400
2014.04.04	05:58:19	09:47:58	21	14	17	400
2014.04.06	07:51:42	08:43:15	5	4	1	400
2014.06.09	04:48:49	09:51:47	14	14	0	400
2014.06.10	04:54:21	09:49:49	5	5	0	400
2014.08.25	23:57:46	04:34:49	4	4	0	400
2014.09.07	00:11:08	04:20:07	2	2	0	400

NOTE.— List of Start and End times, number and quality of exposures. ESO program 092.B-0009 for 2014.02.28, 2014.03.01, 2014.03.02, 2014.03.26, 2014.03.27, and 2014.04.06, ESO program 092.B-0920 for 2014.03.11, 2014.03.12, 2014.04.02, 2014.04.03, and 2014.04.04 and ESO program 093.B-0092 for 2014.06.09, 2014.06.10, 2014.08.25, 2014.09.07. Pre- and post-peribothron measurements are separated by a horizontal line.

and that are unresolved with the current instrumentation (Sabha et al. 2012). Several absorption features from the stellar atmospheres can be recognized in the *HK*-band data. Line emission of ionized species (hydrogen and helium) at the position of the S-stars, and all across the field is also substantial. We refer to the aggregate of all these components as background, and show how it affects the detection of the faint emission of the DSO.

3. Results

In summary, we find that both the line shape and line intensity in 2014 is very similar to that of the previous years. Before May 2014 we find no blue line emission from hydrogen or helium above the noise level. The red-line center has shifted to a higher velocity of about 2700 ± 60 km/s about 40 mas east of SgrA*. In addition we measure the Pa α $\lambda 1.875 \mu\text{m}$ line between atmospheric absorption bands but find that the sky subtracted HeI ($2.05 \mu\text{m}$) is very weak i.e. less than a fifth of the Br γ line emission. In June 2014 our data does not allow use to detect the HeI or Pa α line emission. Peribothron happened in May 2014 and after that we see a in June 2014 blue-shifted Br γ

line about 16 west of SgrA* at -3320 km/s and no red line emission. In June 2014 we find no blue line emission helium, Br γ or Pa α above the noise level.

3.1. Red-shifted pre-peribothron lines

In 2014, the Br γ line emission from the DSO has shifted to a spectral region where the emission and absorption features of the surroundings are very prominent. Moreover, the Pa α and the possible He I lines lie in a wavelength range where the atmospheric absorption plays a main role. Therefore, a proper background estimation and subtraction, as well as an adequate fitting and correction of the tellurics, are critical to detect and measure any emission from the DSO. The latter is expected to change from one day to the next, and also during one observing night if the weather conditions are unstable, but it is approximately the same across the field of view. The former, on the other hand, varies strongly across the field and significantly in periods of about six months, because of the high stellar proper motions. This means that, while the telluric absorption can be, in principle, fitted and corrected using extra observations of stars or sources in the field, the exact shape of the background spectrum at the position of the

DSO cannot be known, but only approximated by using apertures in the field. A carefully calculated approximation to the background leads to a reliable estimation of the spectral properties of the source’s line emission as well as the the spatial position and extension of the DSO emission,

3.1.1. The $Br\gamma$ emission line

Figure 1 shows the spectrum integrated over apertures of radius $0.05''$ at the position where the red-shifted $Br\gamma$ emission from the DSO is strongest. It also shows the background spectra constructed from four different surrounding regions, and the resulting line emission after subtracting them from the source spectrum. On the left-hand panels, the spatial pixels from which the spectra of the source and the background have been extracted are marked with blue crosses and pink filled squares, respectively. The SgrA* position is marked with the big cross. The middle panels display the integrated spectrum at the DSO position (thick blue line) in comparison with the background spectra (thin pink line). The vertical dashed-line at $2.166\ \mu\text{m}$ marks the spectral position of the zero-velocity $Br\gamma$ line. Arrows at $2.076\ \mu\text{m}$ and $2.185\ \mu\text{m}$ indicate the approximate location of the DSO red-shifted He I and $Br\gamma$ emission lines. The inset panel corresponds to the dashed-line box, which is a zoom-in to the spectra in the $2.18 - 2.20\ \mu\text{m}$ range. The arrow in the inset panel marks again the position of the red-shifted $Br\gamma$ line and highlights the importance of the background subtraction to recover the spectral properties of the emission. Because of the change of the spectral slope across the field of view, the overall shape of the spectrum extracted from the background area has to be slightly modified to better fit the continuum in the DSO aperture. To do that, we divide it by a third-order polynomial fitted to the ratio between the source spectrum and the spectrum of the background aperture. This is done using only the spectral windows marked with (green) crosses in the top panel of the middle column. Then, the background was scaled to best match the continuum emission around the spectral location of the $Br\gamma$ red-shifted emission (i.e., at $2.173 - 2.183\ \mu\text{m}$ and $2.195 - 2.220\ \mu\text{m}$). These spectra, with modified slope and scaled continuum, are used as an approximation of the background emission at the DSO position. They re-

produce well most of the features in the source spectrum, as it can be seen in the middle panels. Given that at wavelengths shorter than $\sim 2.08\ \mu\text{m}$ the emission is highly absorbed by tellurics, we did not include this spectral region in the fit of the overall background-spectral shape, but used only the selected spectral windows as described above. For this reason, the background continuum in the source aperture at $\lambda \lesssim 2.08\ \mu\text{m}$ can not be fitted properly and produces an excess of emission in the background-subtracted DSO spectra that can be seen in the right-hand panels. There, the large mismatch observed in the spectra in a range of $0.82\ \mu\text{m}$ around the zero-velocity $Br\gamma$ line is due to strong variations of the ionized hydrogen emission in the central $r \sim 1''$ region. Lines within the telluric absorption region are treated differently to improve their signal strength, see section 3.1.3.

The four examples shown in Fig. 1 correspond to the cases when: 1) The background is created from an aperture of the same size and shape as that of the source, and it is located just beside it. 2) Iris photometry is applied, i.e. the background aperture is a ring around the source aperture. In this case, the inner radius was chosen to be $0.06''$ and the outer radius, $0.11''$. 3) An averaged background is created from a region of radius $0.25''$ at the source position that includes the DSO aperture. 4) The source emission is integrated in a segment of $0.075''$ width taken along the best-fit elliptical orbit with a length of $\sim 0.10''$ (see section 4.1). The background is integrated from the $0.048''$ -width stripes above and below the source area. In all cases the red-shifted $Br\gamma$ line is detected with signal-to-noise ratios between 3.9 (in the second case) and 4.7 (in the third one).

Fitting a Gaussian to the line emission in each case, we find a rather robust determination of the line peak at $2.185\ \mu\text{m}$, i.e., $2700\ \text{km s}^{-1}$ in average with a variation of $60\ \text{km s}^{-1}$. However, as it can be noticed from Fig. 1, the line profile changes depending on the subtracted background. The FWHM of the $Br\gamma$ line, corrected for instrumental broadening, is $730\ \text{km s}^{-1}$ in the first and third cases, $560\ \text{km s}^{-1}$ in the second, and only $240\ \text{km s}^{-1}$ in the fourth one. Averaging over a dozen background-subtracted source apertures the $\text{FWHM}(Br\gamma) \approx 720 \pm 150\ \text{km s}^{-1}$, i.e. the line width is $50 \pm 10\ \text{\AA}$. The line flux changes, in general, by a factor of two due to the back-

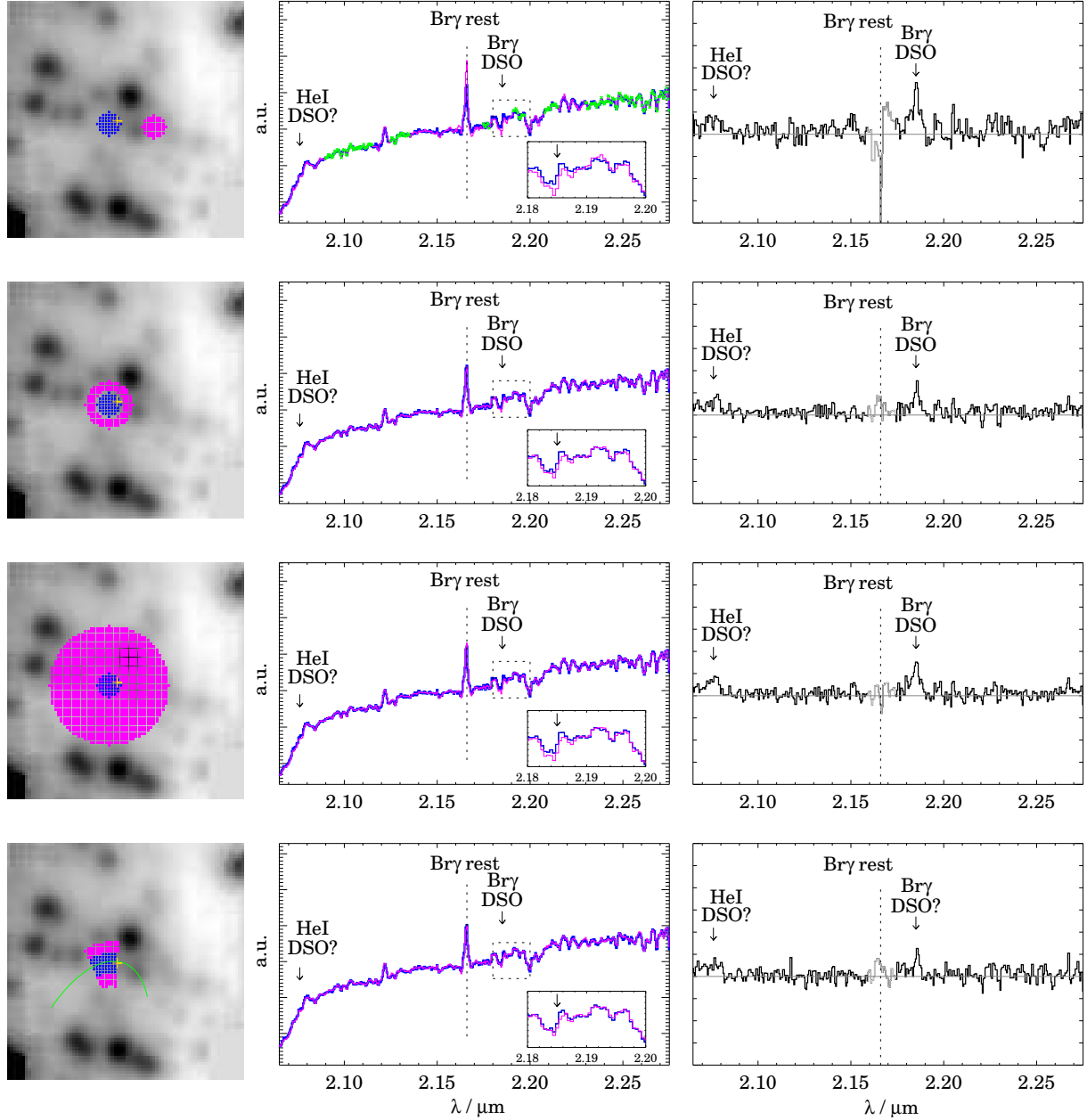


Fig. 1.— $\text{Br}\gamma$ red-shifted emission of the DSO before May at 43mas east and 5mas south of SgrA*. *Left panels:* $1 \times 1 \text{ arcsec}^2$ SINFONI mosaic of the Galactic center region in February to April 2014. DSO (blue crosses) and background (pink squares) apertures are shown. *Central panels:* Comparison between the DSO (thick line) and the background (thin line) spectra. Arrows mark the expected location of the red-shifted He I and $\text{Br}\gamma$ lines. *Right panels:* Results of the subtraction of the background from the DSO spectrum. The baseline is shown in gray. The vertical range of the plots corresponds to one unit in the middle panels. See details in the text. See the electronic edition of the Journal for a color version of this figure.

ground subtraction. In the first three examples shown in Fig 1, it is in the range $3.1 - 6.0 \times 10^{-16} \text{ erg s}^{-1} \text{ cm}^{-2}$, while in the last case it only reaches $1.7 \times 10^{-16} \text{ erg s}^{-1} \text{ cm}^{-2}$. For a distance of 8 kpc to the Galactic center, the average luminosity of the observed red-shifted $\text{Br}\gamma$ line is $1.0 \times 10^{-3} L_{\odot}$, and twice this value when integrating over a larger aperture of radius $r = 0.075''$.

In the last example in Fig. 1 the recovered properties of the emission line are quite different to any other case, although the bulk of the source emission seems to be well within the aperture placed along the orbit, and that it covers a very similar area as the circular aperture used in the first three cases: e.g. the line width in the last case is narrower and the line flux is only $\sim 35\%$ of that measured in any other background-subtracted spectrum. From this analysis, we call for precaution when measuring line properties along predetermined areas in the field-of-view.

3.1.2. Position of the DSO

To confirm the position of the $\text{Br}\gamma$ emission, we removed the background emission in every pixel of the field-of-view following the procedure described above using the spectrum shown in the second example of Fig. 1 as a background - as classical iris photometry makes an unbiased and efficient use of the background in the immediate surrounding of the source. Then we integrated the residual flux in the range $2.181 - 2.193 \mu\text{m}$. The result, shown in the top-left panel of Fig. 2, is an image of the excess flux, compared to the continuum, emitted by the source in this wavelength range. Fitting a Gaussian to this emission in every spatial pixel, allows us to mask the areas where the flux within the line is less than $2\times$ the noise level. When such a mask is applied (Fig. 2, top-right), the location of the DSO shown by its redshifted $\text{Br}\gamma$ emission is clearly revealed. The position of the DSO as indicated by the position of the brightest $\text{Br}\gamma$ peak in Fig. 2 is 8.6 mas south and 41.5 mas east of Sgr A^* .

3.1.3. The He I and $\text{Pa}\alpha$ emission lines

The detection of $\text{Pa}\alpha$ $\lambda 1.875 \mu\text{m}$ and He I $\lambda 2.058 \mu\text{m}$ emission requires modeling of the atmospheric absorption. Although we observed some standard stars during the different runs to use them for the telluric modeling, the sky variation

throughout the nights was large and the corrections unsatisfactory. The alternative is to use a bright star in the field, or a combination of some of them, as tracers of the telluric absorption. Fig. 3 shows the case where the star S2 is used for this purpose. In the top panel, a comparison between the DSO spectrum and that of S2 is shown. The absorption features in the source spectrum around $1.9 \mu\text{m}$ are well approximated, but the overall shape of both spectra differs from each other, as expected from the earlier discussion.

Following the common telluric-correction procedure, the DSO spectrum is divided by the normalized telluric spectrum (in the case of Fig. 3 that of S2). The same correction is applied to the background spectrum. Here, we selected without preference the background shown in the third example of Fig.1. The resulting DSO spectrum, after the background correction, is still very noisy around $1.9 \mu\text{m}$, but hints of the red-shifted $\text{Pa}\alpha$ and He I are visible. The lines are observed with a signal-to-noise of about 2, in the case of helium, and just above one, in the case of $\text{Pa}\alpha$. The fact that $\text{Pa}\alpha$ is not observed with the expected strength (approximately 12 times brighter than $\text{Br}\gamma$, after extinction correction) is probably due to the low elevation of the Galactic center region in February - April which resulted in stronger telluric absorption in this region. We fit the redshifted He I with a Gaussian to obtain the line properties. It peaks at $2.076 \pm 0.078 \mu\text{m}$, i.e. $\sim 2650 \pm 100 \text{ km/s}$ within the uncertainties at the same receding velocity as indicated by the $\text{Br}\gamma$ line. It also exhibits a similar width $\sim 750 \text{ km s}^{-1}$. After correcting for extinction assuming $A_V \approx 26.8 \text{ mag}$, we find $\text{He I} / \text{Br}\gamma \sim 0.6$. consistent with models in which the emission is dominated by optically thin material (Gillissen et al. 2013b; Shcherbakov 2014).

However, this value must be taken with caution, given the low S/N of the lines and the high influence of the tellurics and background corrections in the measured line fluxes.

3.2. Blue-shifted pre-peribothron lines

The blue side of the line emission would be extremely diluted if we observed the source very close to its peribothron position and the radial velocity range would span almost 6000 km/s , significantly broadening the emission line and making it virtually impossible to detect. Only if the time

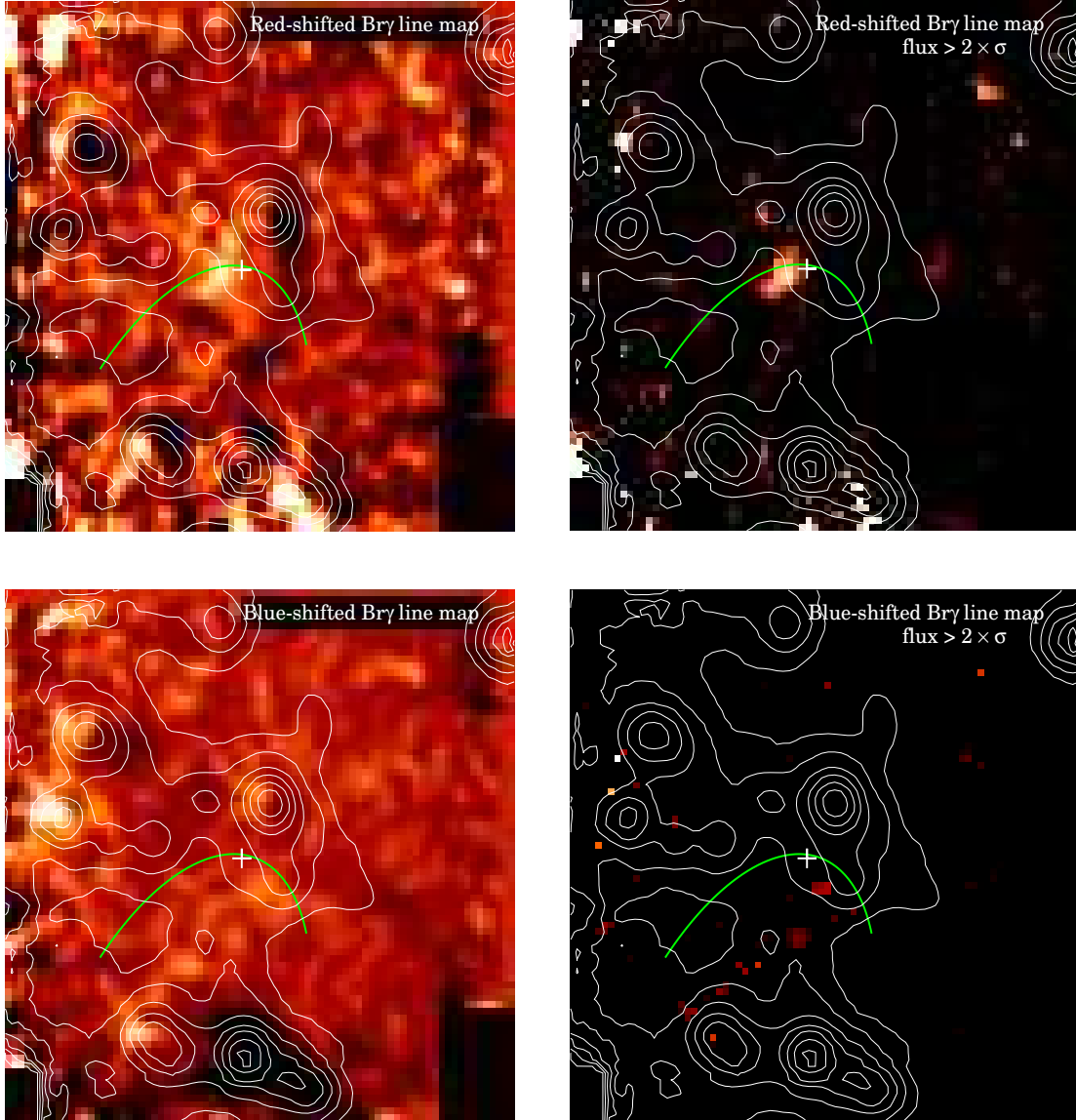


Fig. 2.— $\text{Br}\gamma$ line maps. Panels show $1.0 \times 1.0 \text{ arcsec}^2$ of the Galactic Center region in February–April 2014. The cross marks the position of SgrA*. The thick green line corresponds to the best fit elliptical orbit. The K -band continuum contours depict the brightest S-cluster members. *Top panels:* DSO red-shifted $\text{Br}\gamma$ line map. *Left:* Integrated emission in a range of 120 \AA around $2.185 \mu\text{m}$ after subtracting the background in every spatial pixel of the field-of-view. *Right:* Same as left panel, but showing only emission that is brighter than $2 \times$ the noise level. *Bottom panels:* Blue-shifted $\text{Br}\gamma$ line map. *Left:* Integrated emission in a range of 120 \AA around $2.147 \mu\text{m}$, i.e., around the expected blue-shifted $\text{Br}\gamma$ line emitted by a source approaching us at a speed of 2700 km s^{-1} . The background has been subtracted in every spatial pixel of the field-of-view. The color scale is the same as on the upper panels. *Right:* Same as left panel, but showing only emission brighter than $2 \times$ the noise. See the electronic edition of the Journal for a color version of this figure.

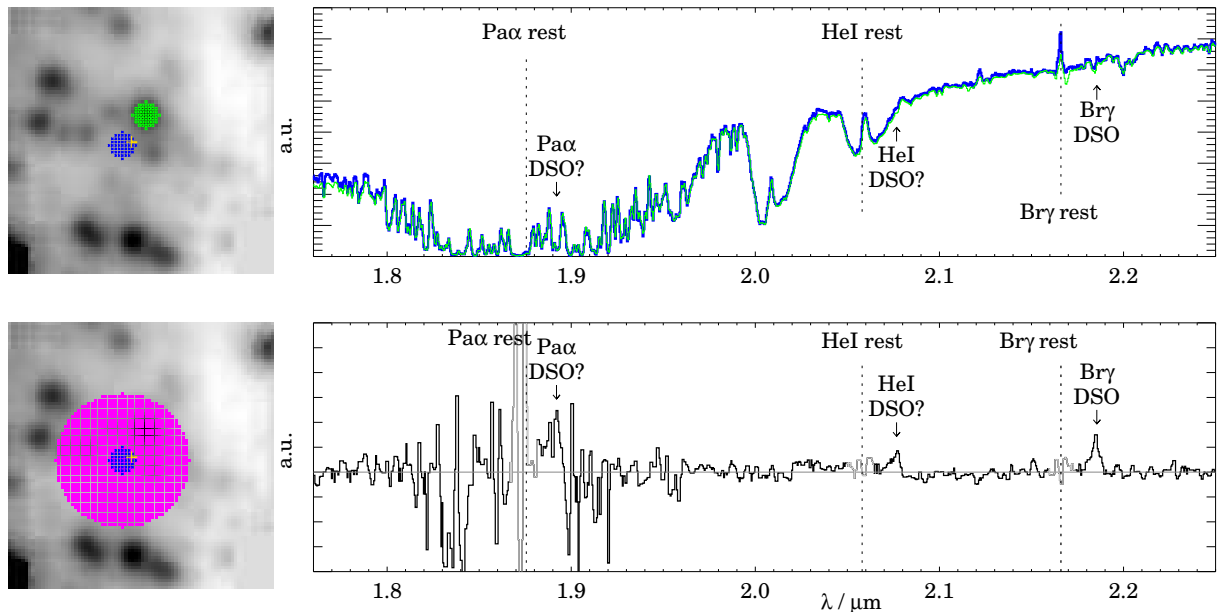


Fig. 3.— The He I and Pa α red-shifted emission of the DSO before May. *Top left*: 1×1 arcsec² SINFONI mosaic of the Galactic center region in February to April 2014. The DSO aperture is marked with blue crosses. The spectrum extracted from the aperture placed on S2, marked with empty green squares, is used to model the telluric absorption. *Top right*: Comparison between the DSO spectrum (thick blue line), and the telluric model (thin green line). The positions of the zero velocity hydrogen and helium lines are signaled with vertical dashed lines, while the expected positions of the red-shifted emission lines from the DSO are indicated with the arrows. *Bottom left*: Same as in left panels of Fig. 1. *Bottom right*: Results of the subtraction of the background from the DSO spectrum, after correcting both spectra for tellurics. Dashed lines and arrows are the same as above. See the electronic edition of the Journal for a color version of this figure.

span for such an event was of the order of a week (depending on the exact orbit) observations immediately after our measurements may have picked up significant blue line emission.

3.2.1. No detected blue Br γ emission

Using a variety of apertures we conducted a systematic search of the DSO blue-shifted Br γ emission along the portion of the orbit which lies upstream of the red emission. As we did not find blue-shifted emission at the pre-peribothron position of the DSO, we extended our search to consecutive positioned apertures upstream the April 2014 pre-peribothron position. Corresponding to the findings of Pfuhl et al. (2014) the blue line emission should have been the brightest line component in our data. If the blue-shifted emission is

compact, and at least half as bright as the red-shifted one, we should be able to detect it with a $S/N \sim 2.5$ or higher.

Following the same approach presented in Sect. 3.1.1., i.e., subtracting background spectra created in different ways from the source spectrum, we aimed to find hints of the blue-shifted component. The DSO spectrum was integrated from an aperture with the PSF size ($r = 0.05''$) that was placed several times in a grid mapping a squared area of $200 \text{ mas} \times 200 \text{ mas}$ with Sgr A* at the north-east corner.

In this way we covered the large area to the west and to the south of SgrA* where the approaching side of the DSO is expected to be found. We also searched for the blue-shifted emission using slightly larger apertures to account for a possibly

more extended emission that could be expected in case the source was not as compact as before the peribothron passage.

Figs. 4 and 5 show two attempts of finding the Br γ DSO emission in two different positions upstream of the best fit elliptical orbit. These are examples of the systematic search for the DSO Br γ emission south/west of SgrA*. The apertures are placed at the position (and one consecutive position) along the orbit at which Pfuhl et al. (2014) and earlier Gillessen et al. (2013b) had reported the detection of blue-shifted line emission.

As in Fig. 1, left panels show the size and position of the background and source apertures, middle panels compare the spectra extracted from them, and right panels present the subtraction of the two. The expected spectral positions of the blue-shifted Br γ and He I are derived assuming the emitting source to approach us after peribothron with a similar speed as the still receding part. The vertical range in the right panels is the same as the one used in Fig.1, and therefore can be directly compared. In case there is a source emitting a blue-shifted line at any of these two positions, the line should be clearly visible in all four rows displayed within one figure. This is because, in these four examples, the source spectrum is extracted from the same region and the only difference must be the signal to noise ratio of the line which depends on the subtracted background (we come back to this point in section 3.2.3). Hence we can rule out that there is a blue line similar to that seen on the red shifted side despite the fact that the source should be similarly compact (see Figs. 1 and 5 in Pfuhl et al. (2014) and comments in our introduction section).

3.2.2. Upper limit for the blue-shifted Br γ line

Another strategy for searching a line emission is, as we did in previous sections, to subtract a background spectrum from the entire data cube and then integrating the remaining flux within narrow spectral windows around the expected wavelength. For this search we used different background spectra and integrated the residual flux in the range 2.143 – 2.151 μm . Fig. 2 (bottom-left) shows one example. We fitted a Gaussian to every spatial pixel to create a mask that selects those places where the flux is less than 2 \times the noise level. In the right panel of Fig. 2 (bottom-right),

such mask has been applied. We see possible hints of a spatially compact source at 37.5mas west and 68.8mas south of SgrA* that is not located on the expected DSO orbit. Looking at the line properties we find that in average the emission is very broad, with FWHM > 2000 km s^{-1} (i.e., larger than 0.015 μm), and centroid at $\sim 2.149 \mu\text{m}$. Assuming that the blue-shifted Br γ line emission is as wide as the red-shifted one, i.e. 720 km s^{-1} , and with a noise in that spectral range of $\sim 2.9 \times 10^{-14} \text{erg s}^{-1} \text{cm}^{-2} \mu\text{m}^{-1}$, we obtain an upper limit for the line flux of $\sim 4.7 \times 10^{-16} \text{erg s}^{-1} \text{cm}^{-2}$, i.e. a luminosity $L(\text{Br}\gamma_{\text{blue}}) < 1.0 \times 10^{-3} L_{\odot}$. Whether this emission is real considering the multiple sources of noise, and whether it has some relation with the DSO is unknown. For the apertures placed along the orbit, the upper limit of a blue-shifted Br γ line-flux is $\sim 2.8 \times 10^{-16} \text{erg s}^{-1} \text{cm}^{-2}$, which is about a half of that of the red-shifted line.

3.2.3. Influence of the selected background

There is no doubt that the subtraction of the background emission plays an important role in the detection of faint line emission. The usage of different background spectra from regions close to the position of interest is an effective tool to discriminate between a source line emission and the unlucky presence of a background feature at the studied wavelength. In the first row of Fig. 6a and 6b we present examples of background that produce a spurious blue-shifted Br γ emission at positions far away from the expected orbit. The panels in the second row of each example show how, after selecting different background spectra, a very good overlap with the source spectrum is obtained and only noise remains after the subtraction. The aperture shown in Fig. 6a is located at the position of the bright blob closest to SgrA* in the bottom panels of Fig. 2. The background subtracted spectrum of this aperture was used above to estimate the upper limit for the blue-shifted line. In this case, the S/N of the feature at $\sim 2.15 \mu\text{m}$ depends strongly not only on the background selected, but also on the way it is scaled and subtracted. As we were not able to produce spurious detections on the red side we conclude that those in the blue may result from an enhanced local variation of the background in this particular spectral range. Based on this analysis, we call for caution when

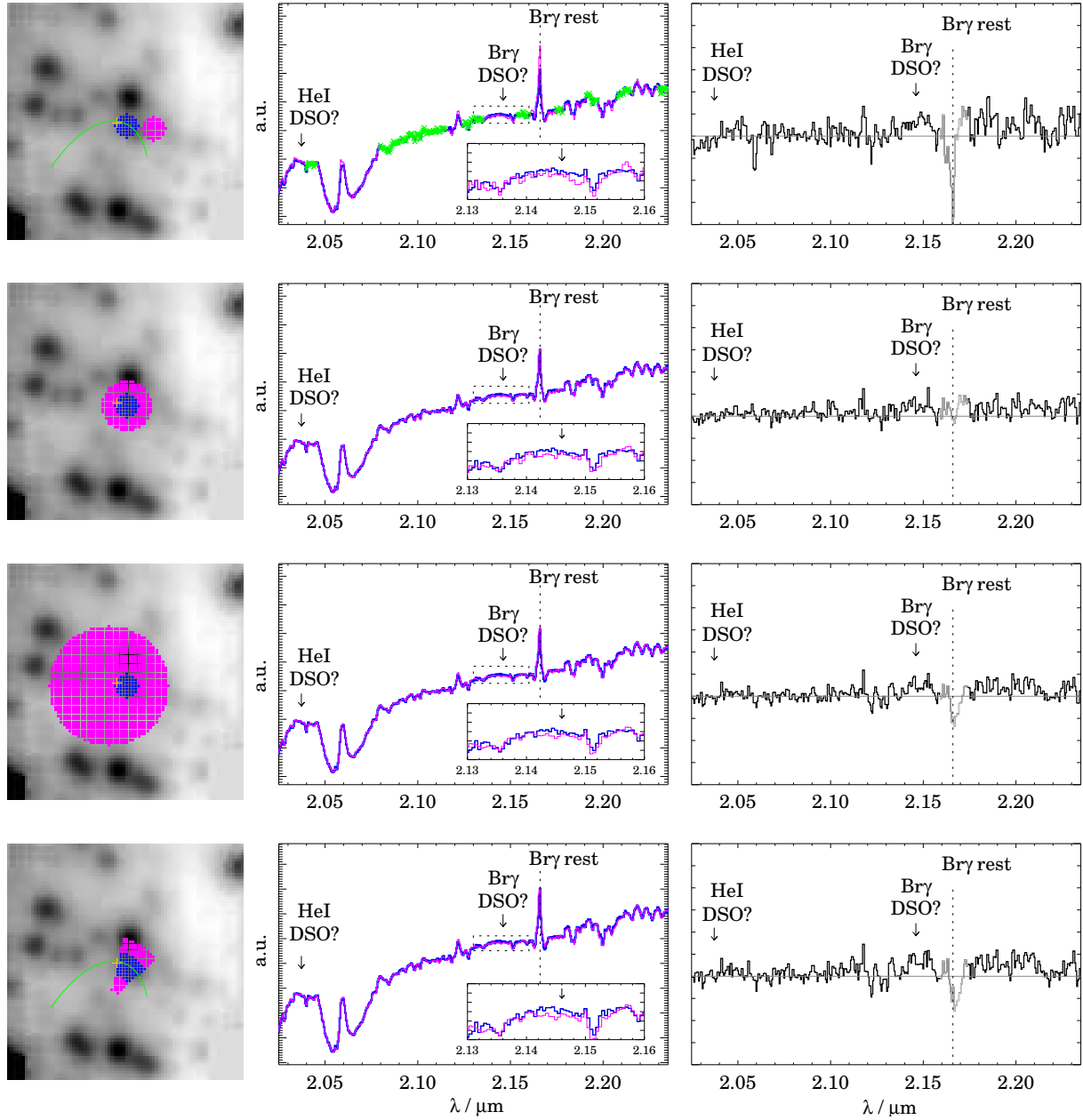


Fig. 4.— Non-detection of Br γ blue-shifted emission before May at a first up-stream position at 43 mas east and about 11 mas south of SgrA*. *Left panels:* Same as Fig. 1. *Central panels:* Comparison between the DSO (thick blue line) and the background (thin pink line) spectra. Arrows at 2.037 μm and 2.146 μm indicate the approximate location of the expected DSO blue-shifted He I and Br γ emission lines, in case the speed of the approaching component was the same as the receding one. The inset panel corresponds to the dashed-line box, which is a zoom-in to the spectra in the 2.13 – 2.16 μm range. The arrow in the inset panel marks again the position of the blue-shifted Br γ line. The spectral windows marked with crosses in the top panel are used to fit the slope of the background spectrum to that of the DSO. *Right panels:* Results of the subtraction of the background from the DSO spectrum. The vertical range of the plots corresponds to one unit in the middle panels and spans the same range as in the right panels of Fig. 1. The zero-line is shown in gray. See the electronic edition of the Journal for a color version of this figure.

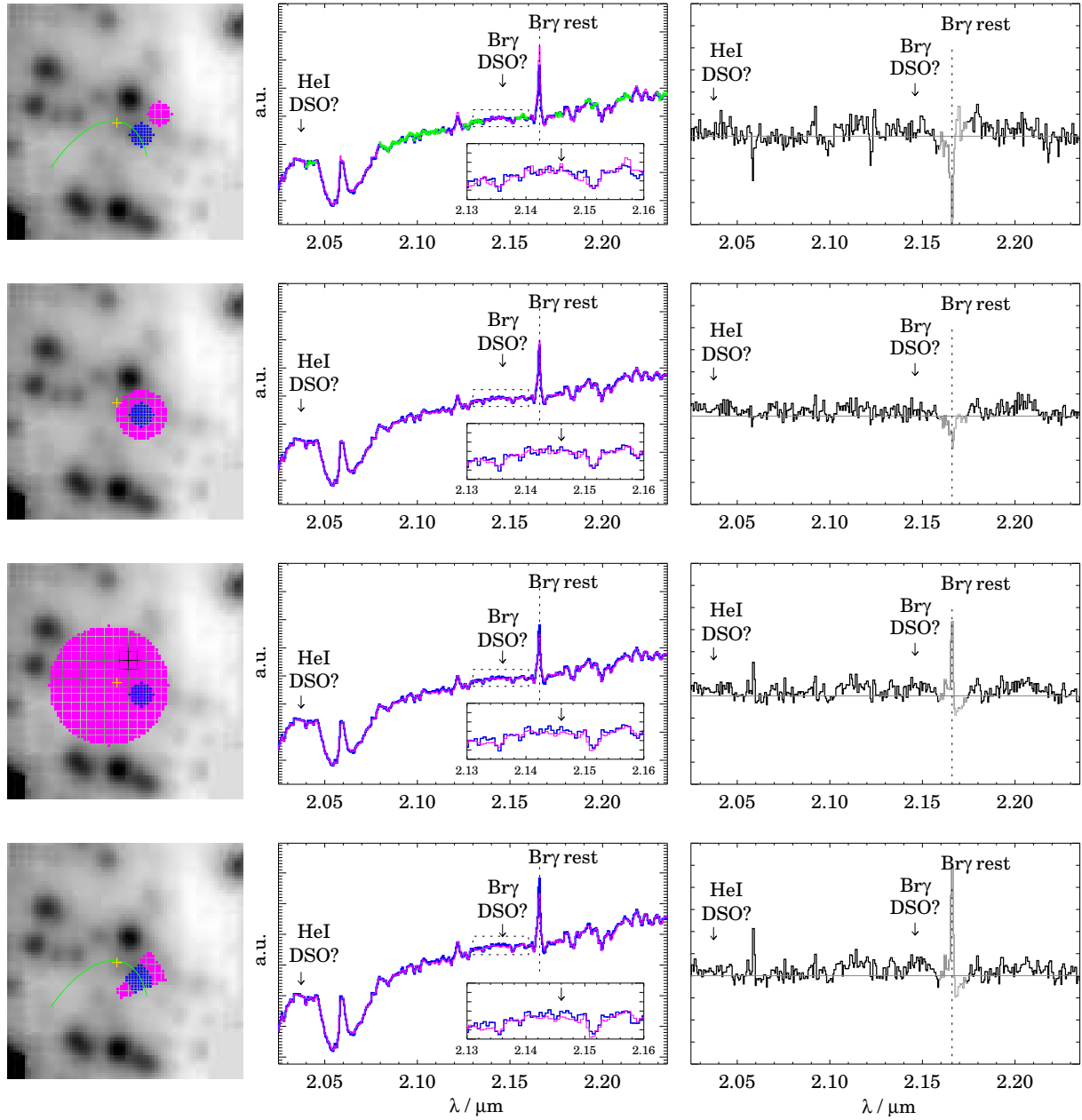


Fig. 5.— Non-detection of Br γ blue-shifted emission before May at a second up-stream position at 103.8 mas West and 50 mas South of SgrA*. Panels and symbols are the same as in Fig. 4. See the electronic edition of the Journal for a color version of this figure.

studying line emission properties of faint sources in crowded fields.

3.3. Blue-shifted post-peribothron Br γ

Fig. 7 shows the spectrum integrated over an aperture of radius $0.05''$ at the post-peribothron in June 2014 at position at 16 mas west and about 6 mas south of SgrA* at a S/N of 2.5 to 3.1 depending on the background subtraction. The line has a blue-shifted center velocity of -3320 ± 60 km/s and after correcting for spectral resolution a FWHM of 15 ± 10 Å. Line flux and width were derived using several background corrections similar to what is shown in Fig.1. The Br γ line luminosity is about $0.4 \times 10^{-3} L_{\odot}$. The narrow line estimate could be a result of the weak line detection, it could also point at a stellar nature of the source (see below).

The excess line emission can clearly be seen even before background subtraction in the inset of the middle top plot in Fig. 7. Based on the post-peribothron observing dates listed in Tab. 1 we assigned an integration time weights epoch of 2014.55 to this measurement. No red-line emission can be claimed for this epoch at this position. In the lower plots of Fig. 7 we show that at that epoch neither red- nor blue-shifted Br γ line emission can be see at our pre-peribothron position (see also the inset of the middle bottom plot). The excess line emission can clearly be seen even before background subtraction in the inset of the middle top plot. The baseline used for this spectrum excludes the region around blue-shifted (2.138 - $2.146 \mu\text{m}$) and the red-shifted Br γ and He line emission (2.175 - $2.190 \mu\text{m}$ and 2.070 - $2.080 \mu\text{m}$) we used at the pre-peribothron position. No red-shifted emission was detected at the post-position. No red-shifted line emission was detected at any position down-stream of the post-peribothron position. In Fig. 8 we show summary spectra at the pre- and post-peribothron positions for 2014. We obtained the spectra using a $0.050''$ radius source and a $0.25''$ radius background aperture centered on the DSO. We subtracted a high-pass filtered version of the spectra that we obtained by replacing the range over which detectable line emission is present (indicated by the three lines at the bottom of the graph) by the mean in the neighboring spectral elements and smoothed the resulting spectrum with Gaussian having a FWHM of 10 spectral resolution elements. The location of the

Br γ rest emission is indicated by a vertical dashed line.

An important question is that of the size of the line emission region and possible velocity gradients across the DSO. To investigate this we obtained line maps of the Br γ emission. In Fig. 9 we show maps of the DSO in its Br γ line emission for the times before (epoch May 2010.45² and April 2014.32) and after (epoch 2014.55) the peribothron. For the brightest and least confused Br γ line maps for May 2010 (Fig. 9) we find a geometrical mean FWHM of 6.5 pixels. For the star S2 we find a FWHM of 6.2 pixels. With 12.5 mas per pixel this gives an upper limit on the deconvolved FWHM source size of 24 mas. The centroid positions of the emission line maps of the left half, right half and full line in milliarcseconds relative to the position of the full line map centroid position are given in Tab. 2. Under the assumption that differences in the relative positions of the red- and blue-half of the single line Br γ emission line map can be interpreted as being due to a velocity gradient of a tidally stretched source we find for all epochs an upper limit of the corresponding source size of 15 mas. This implies that the source emitting the bulk of the Br γ line is very compact and we adopt the value of 15 mas as an upper limit on the line emitting FWHM source size. This is consistent with the analysis of L'-band continuum images by Eckart et al. (2013) showing that $>90\%$ of the DSO emission at $3.8 \mu\text{m}$ wavelength is compact (FWHM ≤ 20 mas) and only up to 10% of the flux density of the DSO can be extended on the scale size of the PSF. Our size limit is also consistent with the upper limit of 32 mas presented by Witzel et al. (2014). These size estimates are all smaller or at the lower bound of the 2008-2013 size estimate of 42 ± 10 mas Gillessen et al. (2013b). Our adopted Br γ source size corresponds to 120 AU at a distance of 8 kpc, i.e. it is of the close to the peribothron distance of the source. However, it is still about 50 times larger than the estimated size of an optically thick dust shell of a $2M_{\odot}$ star of about 2.6 AU Witzel et al. (2014).

4. Discussion

The fact that we found red-shifted Br γ emission at the pre-peribothron position but did not detect

²SINFONI data from ESO program 183.B-100

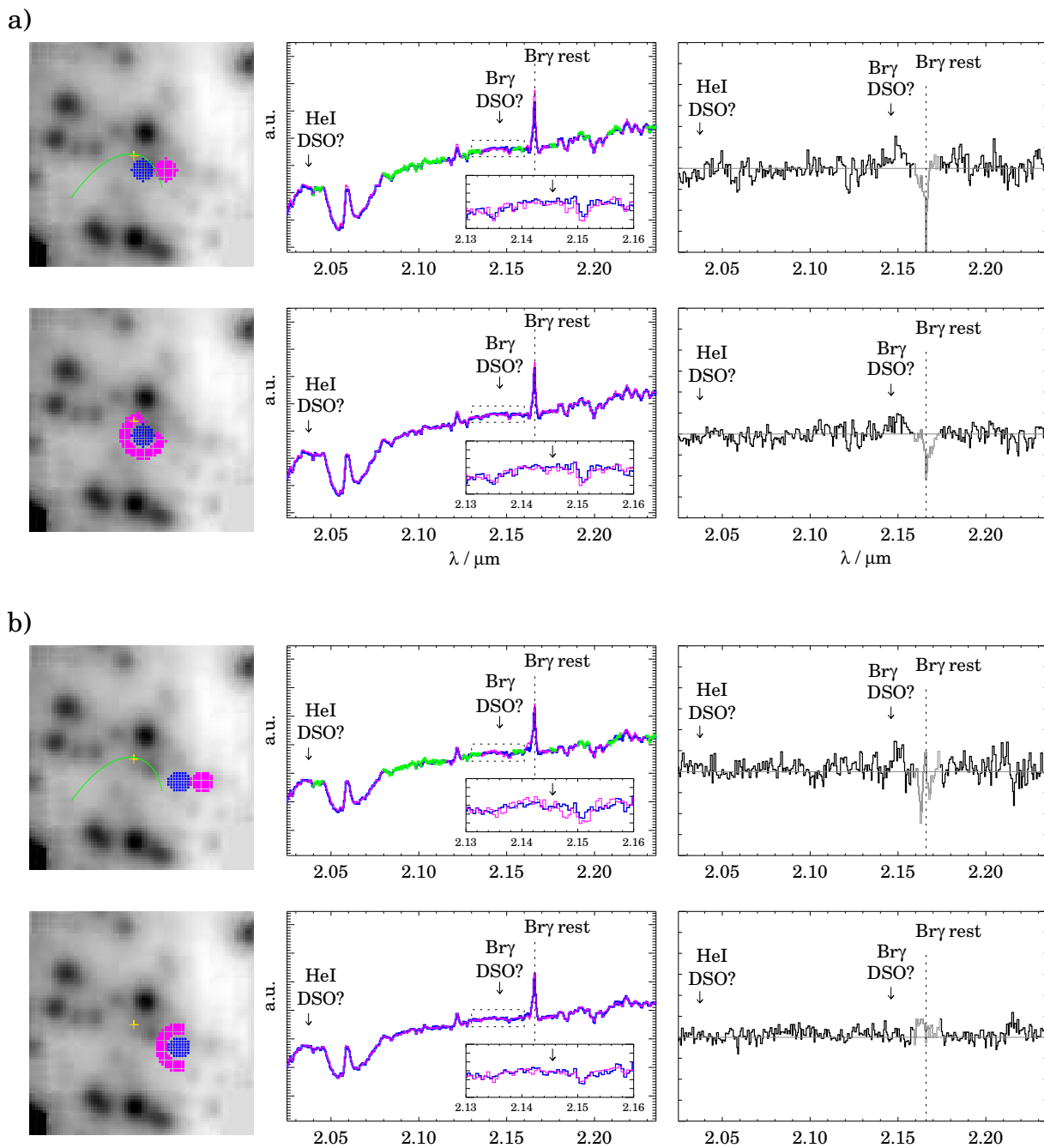


Fig. 6.— Spurious blue-shifted $\text{Br}\gamma$ emission due to background selection. Panel descriptions are the same as in Fig. 4. The two shown cases correspond to sources at *a)* 37.5"/mas west and 68.8"/mas south of SgrA*, and *b)* 200 mas west and 100 mas south of SgrA*. See the electronic edition of the Journal for a color version of this figure.

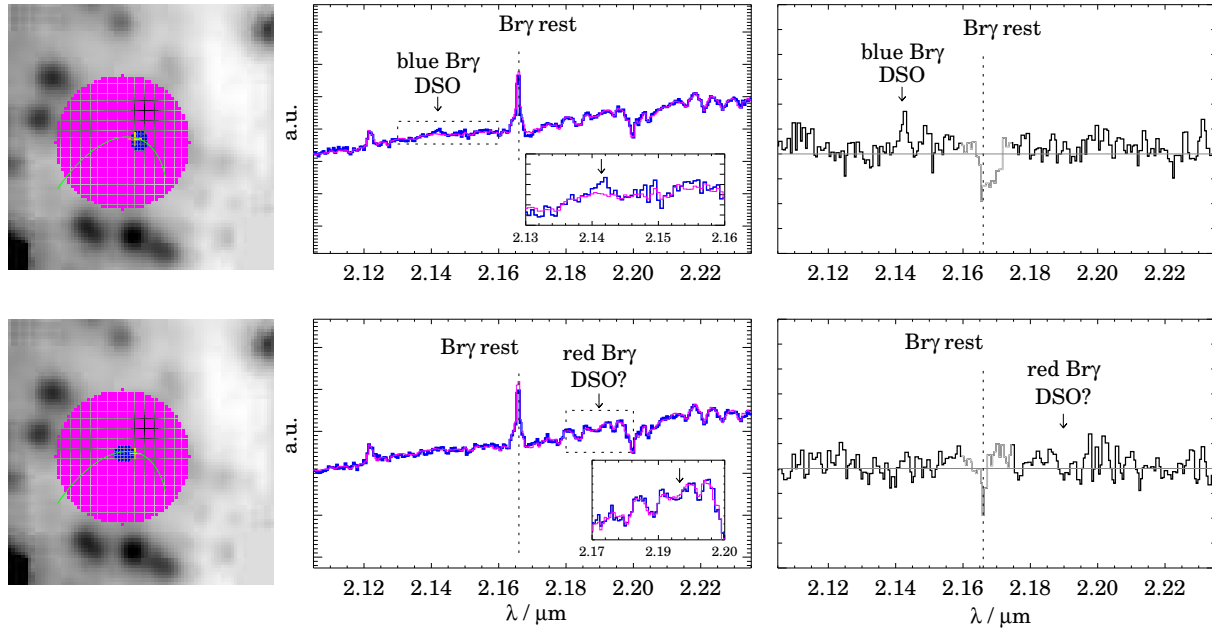


Fig. 7.— $\text{Br}\gamma$ line emission after peribothron passage: Top: Blue-shifted $\text{Br}\gamma$ emission detected at 12 mas west and about 5 mas north of SgrA*. Bottom: No red- or blue-shifted $\text{Br}\gamma$ emission detected at our pre-peribothron position at 43 mas east and about 5 mas south of SgrA*. See the electronic edition of the Journal for a color version of this figure.

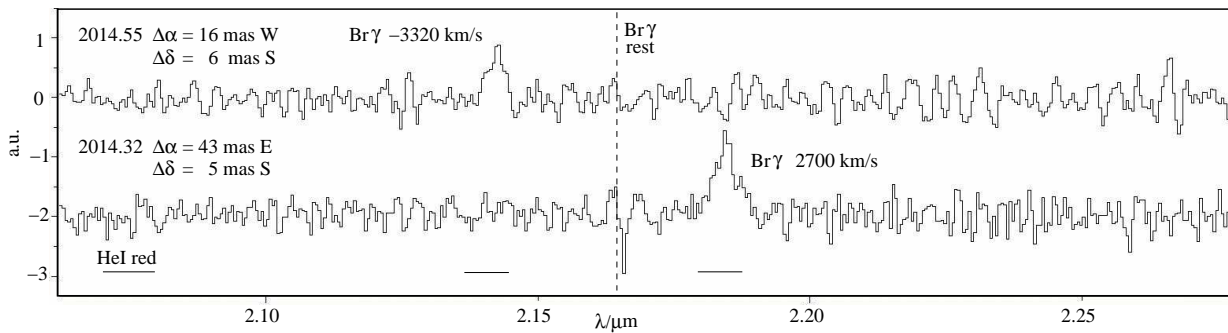


Fig. 8.— Summary spectra at the pre- and post-peribothron positions for the April and June epoch 2014. See details in text.

any blue-shifted emission up-stream (in sections 3.2.2 and 3.2.1 we only show two examples - we probed several positions along the orbit) and vice versa (section 3.3) has implications on the orbit and on the DSO model.

4.1. The orbit

Based on L-band imaging an infrared excess source within the central cluster of high velocity S-

stars was found to approach the immediate vicinity of SgrA* (Gillessen et al. 2012). In addition, $\text{Br}\gamma$ line emission was reported by Gillessen et al. (2013a) and Phifer et al. (2013). In Eckart et al. (2013) we report the identification of K-band emission from a source at the position of the L-band identifications. Gillessen et al. (2013b) report a marginally spatial extension of the $\text{Br}\gamma$ line emission in their SINFONI data and find an intrinsic Gaussian FWHM size of 42 ± 10 mas (using

TABLE 2
CENTROIDS OF DSO LINE MAPS

epoch	blue half		full line		red half		red-blue half	
	[mas]	[mas]	[mas]	[mas]	[mas]	[mas]	[mas]	[mas]
April 2014	-6.75	-7.63	0.0	0.0	+6.25	+6.00	+13.0	+13.6
June 2014	-0.25	+4.25	0.0	0.0	+4.50	-3.88	-4.75	-8.13
May 2010	-4.63	-6.00	0.0	0.0	+4.13	+4.63	+8.75	+10.63

NOTE.— For the single emission line we measured at both 2014 and the May 2010 epochs we list the line map right ascension and declination centroids for the blue and red half of the corresponding single line in milliarcseconds with respect to the 'full line' position. In the last two columns we list the positional difference between the red- and blue-half centroid positions. One pixel corresponds to 12.5 mas.

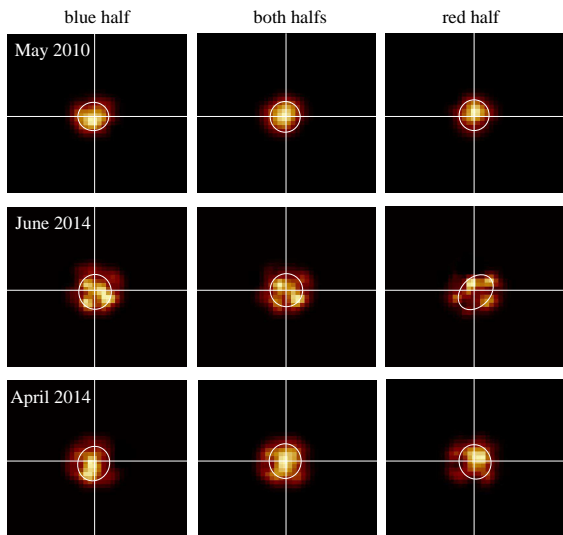


Fig. 9.— Maps of the DSO in its $\text{Br}\gamma$ line emission for the April 2014.32, June 2014.55 and May 2010.45 epochs. The maps are $0.5'' \times 0.5''$ in size. The centroid data are given in Tab. 2. See the electronic edition of the Journal for a color version of this figure.

2008-2013 data). Given the peculiar orientation of the source estimated orbit, precise estimates of the source elongation along the orbit are difficult to obtain. Combining these observational facts indicated that a dusty object - possibly associated with a stellar object - is on an elliptical orbit around SgrA*. The observational data were also used to derive the orbit of this object and to predict its peribothron transition. Due to the presumably high ellipticity of the orbit only very

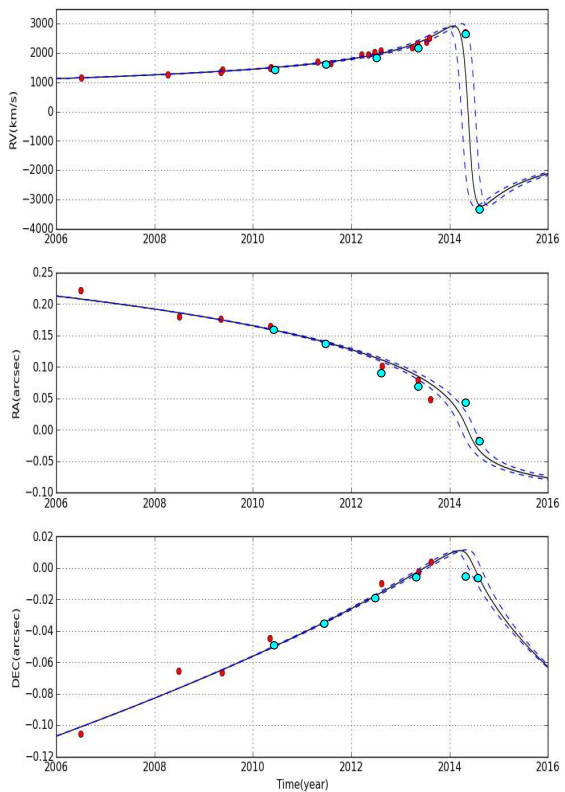


Fig. 10.— Right ascension, declination and radial velocity of the DSO together with the best orbital fit we obtained. See details in text.

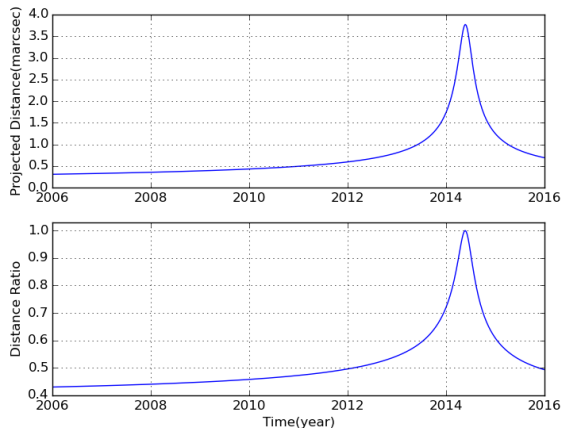


Fig. 11.— Orbital projection effects: Top: The evolution of the projected separation between two neighboring points of arbitrary 0.5 units in 2011. Bottom: Foreshortening factor of any structure along the orbital extent as a function of time.

weakly curved sections of the orbit were available and first predictions of the peribothron transition time in 2013 (Gillessen et al. 2012) proved to be incorrect. The inclusion of (or even restrictions to) the $\text{Br}\gamma$ line emission resulted in new predictions for early 2014 (Gillessen et al. 2013a; Phifer et al. 2013). The fact that the telescope point spread function (PSF) in the L-band is intrinsically larger and therefore more susceptible to diffuse extended emission is probably the main reason for this discrepancy.

However, the predicted interactions of the gas and dust with the strong gravitational field of SgrA* have shown that the gas itself may also not be a good probe of the exact orbital motion. This is supported by the spatial extent and the velocity gradient across the $\text{Br}\gamma$ line emission. It is also highlighted by the expected interaction of the DSO with the ambient medium and the gravitational field. Therefore, even though the recently derived $\text{Br}\gamma$ based orbital solutions are in reasonable agreement (Meyer et al. 2014a,b), the orbital elements may still be uncertain.

Using results from our measurements with SINFONI obtained between February and September 2014, SINFONI archive data as well as the published Keck data (Meyer et al. 2014a,b) we

revisited the determination of the DSO orbit. Given that the red emission is only about 40 mas East of SgrA* and at a radial velocity of about 2700 ± 60 km/s and blue emission about 30 mas West of SgrA* at -3320 km/s we obtained a new orbital solution which places the peribothron passage at 2014.39 ± 0.14 , a bit later but close to 2014.2 as derived earlier (Meyer et al. 2014a,b). Otherwise, the orbital elements are very similar to the ones derived earlier. In Fig.10 we show the fit to the data we used. The formal statistical uncertainties of the positional measurements are of the order of a few milliarcseconds. However, the systematic effects probably limit the uncertainties to a value closer to ± 10 mas. (see Fig.9 by Eckart et al. (2012b)). For the 2014 data presented here the exact positioning of the $\text{Br}\gamma$ line emission critically depends on the transfer of the SgrA* position as obtained during a 3 mJy flare we observed in March to all the other 2014 epochs. This was done using the known position and velocity of the southwards moving bright star S2 that is currently about $0.11''$ north and $0.06''$ west of SgrA*. For the radial velocities we assume the value of 60m/s we adopted for the SINFONI data. The light blue filled circles indicate our per- and post-peribothron 2014 data points we obtained using SINFONI at the VLT. The other light blue filled circles show the results from our re-reduction of earlier SINFONI VLT archive data. Red filled circles represent data as obtained with the Keck telescope and published by Meyer et al. (2014a,b). The dashed lines indicate the approximate 1σ uncertainty of the fit. The orbital elements are given in Tab. 3. With the ellipticity $e=0.976$ and the half axis length of 33 mpc we obtain a peri-center distance of about 163 AU. Which is comparable to previous estimates (Pfuhl et al. 2014; Phifer et al. 2013; Meyer et al. 2014a) and indicates that even if the DSO is an embedded star, its outer shell may very well be subject to tidal disruption (see also section 5 and Eckart et al. 2013; Witzel et al. 2014).

In Fig. 11 we show the size evolution of structures along the orbit under the assumption of freely moving neighboring points. In the case of the DSO the shapes of the two graphs by chance look very similar. We verified that they are indeed very different for other orbital configurations, i.e. lower inclination or the apobothron pointing

towards the observer. The top graph shows the evolution of the projected size of a source moving along the orbit. The bottom graph shows the same quantity divided by the actual three dimensional size of the source, i.e. the amount of foreshortening that the observer needs to correct for. Both graphs demonstrate that close in time to the peribothron passage the foreshortening correcting is close to unity and that the DSO can be seen close to its full extent along the orbit.

4.2. Tidal interaction with SgrA*

The way in which the gas cloud will get disrupted depends on the exact orbit and the nature of the DSO, i.e., if there is a stellar core or not. If there is a central star, then higher mass (typically ten solar masses) objects may retain more of the gas and dust mass in their corresponding Roche lobe than low mass objects (one solar mass and below). This is discussed in Eckart et al. (2013). Recent model calculations for cases with a stellar core or even a binary core have been published by Zajaček et al. (2014)

A tail that is physically connected to the DSO has been reported by Gillessen et al. (2012; 2013a; 2013b). Eckart et al. (2013; 2014a), Phifer et al. (2013), and Meyer et al. (2014a) have questioned this physical association of the DSO with the extended Br γ and dust continuum emitting filament about 0.3" SEE of SgrA*. The rather extended shape of this emission close to rest frame velocities may very well be associated with the Galactic center fore/back-ground features which are numerous in this region. It also does not follow precisely the orbital track of the DSO. Especially at velocities close to rest frame velocities the general central cluster region is very crowded. Hence, despite an indication of very faint emission pointing towards this general region 0.3" SEE of SgrA* a physical association of the bright 'tail' emission is still questionable.

If the DSO is a pure very compact and solitary gas and dust cloud, then it formed through a special process at a very special place and time. As speculated by Pfuhl et al. (2014) it must have formed between 1990 and 2000. Unless one claims, as a further special feature of this source, that it has been formed at a 100% efficiency, some relics and further similarly compact dust filaments or bullets must have been formed along that process.

These have not been identified yet. It also must be noted that during the 1990-2000 time interval the entire Galactic center region was under detailed investigation in the entire NIR/MIR and radio wavelength band with observing runs closely placed in time. No special event in the mini-spiral to the south-east of SgrA* had been reported then.

It has been noted that the thermal instability can explain in a natural way the pressure equilibrium between the hot and the cold plasma in the mini-spiral region (Czerny et al. 2013; Róžańska et al. 2014).

Hence, this process is relevant for the possibility of survival of the infalling clouds in the region, and it also allows us to estimate the typical size of clouds. In fact, clouds as large as 10^{14} - 10^{15} cm (0.001-0.01 light years) can persist. From the dominating optically thin DSO line emission a total mass of the clouds of $\simeq 10$ Earth masses can be derived, depending on strength of the ambient radiation field. This agrees with recent results (Shcherbakov 2014) suggesting the mass of the DSO/G2 cloud to be within the range 4 - $20M_{\oplus}$. Naturally, this would be upon the assumption of a core-less cloud scenario, whereas the mass estimates do not apply if a star is embedded within the cloud. It turns out that clouds located in the distance exceeding ~ 0.05 pc from Sgr A* can survive a few hundred years, which means that the cooling and evaporation time is shorter than the free-fall time onto the black hole.

Gillessen et al. (2013b) and Pfuhl et al. (2014) suggest that 13 years prior to the DSO peribothron passage the source G1 went through its on an orbit connected to the current DSO orbit. Dust heating of G1 would then explain the moderate infrared excess of 0.3 K-band magnitudes of the star S2 in 2002 (appendix by Pfuhl et al. 2014) as it passed close to SgrA* and G1. However, with Sabha et al. (2012) we have shown that over timescales of a few months to a few years - especially close to the center - serendipitous sources can frequently be formed due to density fluctuations of the background stars in the central arc-second.

The DSO is supposed to be on a similar orbit as the G1 source (Pfuhl et al. 2014). However, up to this point, as it is approaching peribothron, the DSO has not shown any increase in K- or even L-band flux density that could be attributed to dust

heating. In fact, while approaching SgrA* in 2013, the L-band identification of the DSO has been lost (Pfuhl et al. 2014). This can in part be attributed to confusion. To some extent diffusion or destruction of dust as the source entered the immediate surroundings of SgrA* may be responsible as well, but certainly no brightening of the source in its K- or L-band emission has been observed.

Until now several models place a star at the center of the DSO (Murray-Clay & Loeb 2012; Eckart et al. 2013; Scoville & Burkert 2013; Ballone et al. 2013; Phifer et al. 2013; Zajaček et al. 2014). An at least partial tidal disruption is also expected if the DSO is an embedded star. A Roche description of the SgrA*/DSO system (Eckart et al. 2013) suggests that a more massive central star will lose less of the gas and dust from the central few AU than a solar mass type star or a dwarf. Simulations of compact systems by Zajaček et al. (2014) support this finding as well (see also section 4.5).

For source sizes that are much smaller than the peribothron distance with Jalali et al. (2014) we have shown that at the peribothron position the gaseous source volume is compressed by at least a factor 2 due to gravitational focusing. This results in the fact that before and after peribothron the source stays relatively compact despite the influence of possible turbulences and shocks that may be induced due to shearing gas streams close to peribothron. Depending on the density of the overall environment hydrodynamic interactions with the ambient material set in well past peribothron. This is consistent with all hydrodynamic and particle simulations that have been used to predict the future development of the DSO or similar sources (e.g. Zajaček et al. 2014; Burkert et al. 2012; Schartmann et al. 2012; Jalali et al. 2014).

4.3. Interactions with the ambient medium

If the DSO passes through an accretion wind from SgrA* it may develop a bowshock. In case it is indeed a dusty star, then one may expect to see cometary source structures quite similar to the sources X3 and X7 which are in the overall mini-cavity region just south of SgrA* at a projected distance of 0.8'' and 3.4'' (Mužić et al. 2010). In mid-2014 the DSO is well within a sphere of hot gas surrounding Sgr A* out to ap-

proximately the Bondi radius ($\approx 10^5 R_S$). As a dusty source, the DSO can therefore be regarded as an obvious probe for strong winds possibly associated with SgrA*. However, there is no clearly resolved structure that can be considered as a bowshock, although the DSO is already closer to SgrA* than X3 and X7. This may indicate that the wind from SgrA* is highly non-isotropic, possibly directed towards the mini-cavity (Mužić et al. 2010) and that the DSO has not yet passed through that wind. However, the mass load of such a wind (due to the radiatively inefficient accretion mechanism) may not be high enough to allow for the formation of a prominent cometary tail structure. The detailed density profile for the central region of the radiatively inefficient accretion flow is difficult to obtain. Methods are rather indirect and accretion model dependant (Baganoff et al. 2003; Marrone et al. 2007; Wang et al. 2013). However, Eckart et al. (2014b) have pointed out that the smaller size compared to X3 and X7 may be due to the higher particle density within the accretion stream close to SgrA* (e.g. Shcherbakov & Baganoff 2010).

4.4. Flare activity

A possibly efficient probe of the interaction of the DSO with its ambient environment or with the black hole itself is monitoring the flux density originating from the central few tenths of an arc-second. However, the results of these efforts have not been very revealing so far.

The NIR flare activity we observed through SINFONI during the peribothron approach in 2013/14 is in full agreement with the statistical expectations as we described them with Witzel et al. (2012). There was no exceptional activity, with 3 flares of a few milli-Jansky strength.

If the DSO would develop a bowshock while approaching the immediate environment of SgrA* then this event might lead to shock accelerations of electrons and to correspondingly strong excursions in the radio emission. However, the strength of these emission peaks depends critically on the size of the bowshock and early estimates of the order of a 1-20 Jy in the decimeter to short centimeter wavelength range had to be revised to values of the order of 0.01-0.2 Jy (Narayan et al. 2012; Sądowski et al. 2013; Crumley & Kumar 2013). Despite a dense monitoring program with the

TABLE 3
ORBITAL PARAMETERS FOR THE DSO

e	a (mpc)	i (deg.)	Ω (deg.)	ω (deg.)	T (yrs)	P (yrs)
0.976±0.001	33.0±3	113±1	76±8	94±8	2014.39±0.14	262±38

NOTE.— The orbital parameters and their uncertainties have been derived on the basis of the UCLA measurements and the April 2014 data point we obtained using SINFONI at the VLT. We assume a distance of 8 kpc and a black hole mass of $4 \times 10^6 M_{\odot}$.

VLA (Sjouwerman & Chandler 2014) strong radio flares have not yet been reported and the now predicted strength of the variability would be in the normal range of the flux density variations observed towards SgrA* (e.g. Markoff et al. 2001, 2007; Eckart et al. 2012a).

So far in the X-ray observable $\geq 2\text{keV}$ band no elevated continuum flux density level or extraordinary X-ray variability has been reported (Haggard et al. 2014). Such an extra emission would have been expected to originate from the shock-heated gas (Gillesen et al. 2012).

Although SgrA* is extremely faint in the X-ray bands, it is strongly variable in this domain of the electromagnetic spectrum (Baganoff et al. 2003, 2001; Porquet et al. 2003, 2008; Eckart et al. 2012a; Nowak et al. 2012; Degenaar et al. 2013; Barrière et al. 2014; Mossoux et al. 2014; Neilsen et al. 2013). The statistical investigation of the near-infrared variability by Witzel et al. (2012) suggests that the past strong X-ray variations are potentially linked with the origin of the observed X-ray echos (Revnivtsev et al. 2004; Sunyaev & Churazov 1998; Terrier et al. 2010; Capelli et al. 2012). Assuming an underlying Synchrotron Self Compton (SSC) process the NIR variability can in fact explain the required X-ray flare fluxes as natural and non-exceptional phenomenon of the source. Therefore, SgrA* is the ideal extremely low accretion rate target that allows us to study this particular phase in which apparently most super massive black holes spend their lifetime. Phenomena like the passage of the DSO may dominate the variability of objects in this phase throughout the electromagnetic spectrum.

While the DSO is a very compact continuum and line emitting source (see section 3.3 and

Eckart et al. (2013)) its peribothron distance is rather small (see section 4.1). Hence it is still an open question if and when some activity of SgrA* is triggered by the DSO fly-by.

4.5. The DSO as a young accreting star

Large line widths are common amongst pre-main sequence stars including both T Tauri stars (with an age of about $10^5 - 10^6$ years) and proto-stars (with an age of about $10^4 - 10^5$ years) with an infalling envelope that forms a disk close to the star. Bertout (1994) already pointed out that Doppler broadening from pre-main sequence stars may range roughly from 50-500 km/s in the course of the accretion phase. As an example, hydrogen recombination and Na D line profiles of several 100 km/s in a number of pre-main sequence stars (e.g. T Tau, DG Tau, DR Tau, AS205, SCrA) are shown. The M0V classical T Tauris star LkCa-8 (IP Tau) (Wolk & Walter 1996; Moto’oka & Itoh 2013) has a 600-700 km/s Br γ linewidth (Edwards et al. 2013) quite comparable to the width currently found for the DSO. Another case of a low mass star with exceptionally large line widths is DK Tau A with an 800 km/s wide line (Eisner et al. 2007). It is listed by Herczeg & Hillenbrand (2014) as a K8.5 star with a mass of $0.68 M_{\odot}$.

Without doubt the Br γ line traces high excitation regions, however, in the case of young embedded proto stars it is currently unclear, whether these regions are associated with accretion funnel flows, the jet base (Davis et al. 2011) or less collimated ionized winds. All of these elements can contribute to the emission and the large observed line width. In the case of the DSO there are several mechanisms that can contribute to a large line

width.

i) Contribution from collisional ionization in a bowshock: A possible origin of a broad wide Br γ emission line was discussed by Scoville & Burkert (2013) on the basis of the bowshock model that is relevant for the supersonic motion of the object through the hot ambient ISM emitting X-rays. They show that Br γ emission may arise from the collisional ionization and the gas cooling in the narrow but dense cold ($\sim 10^5$ – 10^6 K) and shocked layer of the stellar wind. The high densities ($\sim 10^8$ cm $^{-3}$) in this layer can explain the observed emission measure.

ii) Contribution from wind drag in a bowshock: The large increase in FWHM line width from 137 km/s in 2006 to 730 km/s in 2014 could also be related to the increase in orbital velocity from about 1200 km/s to almost 9000 km/s at peribothron. Discussing the emission from photoionized stellar wind bow shocks Cantó et al. (2005) calculate the change of velocity in the thin shocked layer that develops while the source is moving through the ISM. In the context of the DSO this effect has not yet been discussed before. In their equations (19) and (33) they approximate the dependence of that velocity as $v_{sl} \propto v_w \times f(v_a, R, \theta, \phi)$. Here v_{sl} is the velocity in the shock layer, v_w is the stellar wind velocity, v_a is the velocity relative to the ISM. The radius R and the angles θ and ϕ describe the geometry of the shock front. It is the change of v_{sl} across the shock front that may contribute to the observed Br γ line width. The analytic solution of Wilkin (1996) for the thin steady-state bow-shock layer yields the estimate for the shock-layer velocity $v_{sl} \approx 2v_a\theta/[3(1+v_a/v_w)]$ close to the symmetry axis, where the angle θ is small. The ratio of this velocity at the same θ , but different epochs, 2006 and the peribothron crossing, yields $v_{sl}^{per}/v_{sl}^{2006} \approx 1.07$ – 1.26 for the terminal wind velocities of 100–400 km/s, respectively. Thus, the increase in velocity by about 10% could be contributed by wind drag in a bow-shock layer.

iii) Contribution from stellar or disk winds: There can also be a contribution to Br γ emission from the gaseous inner disk, stellar wind, stellar-field driven wind (X-wind) or disk wind (Lima et al. 2010) that can originate from the corotation radius to several astronomical units (see Kraus et al. (2008), for discussion and their Fig. 1). Günther (2011) shows that for classical

pre-main sequence stars, wind velocities of a few hundred km/s can occur.

iv) Tidal contribution: The increase in FWHM of DSO would then be caused by the tidal stretching and perturbation of the accretion disk, especially close to the peribothron, which would consequently lead to larger velocity dispersions of inflow and outflow streams. Simple considerations analogous to the computation of tidal compression presented by Jalali et al. (2014) show the increase of velocity deviation. There are several ways to assess the importance of tidal stretching of the DSO along its orbit from our data:

α) If the total pre-peribothron linewidth of about 720 km/s was dominated by tidal stretching then a minimum source size of about 65 mas is expected based on the mean slope of 1000 km/s over a projected orbital path of about 90 mas (i.e. ~ 11 km/s/mas) within the past two years.

β) Attributing the 2008-2013 size estimate of 42 ± 10 mas Gillessen et al. (2013b) to the year 2013 and assuming a free gas cloud subjected to orbital stretching along the orbit we find that the source should be 5-8 times larger, i.e 210 mas to 336 mas, close to peribothron. We cannot confirm such a large size from our Br γ line maps in Fig. 9 (see also Tab. 2).

γ) The separation of apparently simultaneously observed extreme velocity components of G2 close to the peribothron passage (Fig.1 and Fig.15 in Gillessen et al. (2013b); Pfuhl et al. (2014) which is consistent with a cut through their pv-diagram in Fig.1) implies a size between 90 mas and 150 mas along the orbit. With our data we only see a single lined DSO either red- or blue-shifted with a diameter of < 20 mas and, given the low foreshortening (section 4.1 and Fig. 11), we cannot confirm the presence of multiple sources or a large source extent (see section 3.3 and Fig. 9).

δ) We measured very close to the points at which extreme orbital velocities in the red and blue can be observed. At these positions for an extended tidally stretched source the emission previously blue of the source center will become red-shifted and blue-shifted, respectively. Hence a linewidth that can be up to a factor 2 narrower is expected. However, the post-peribothron linewidth is about a third of the pre-peribothron value, and the small source sized are in conflict with an extended tidally stretched source. In addition the orbital

compression expected for such a scenario would imply a larger line width and a higher line flux density due to the increased density of the emitting gas volume. Instead for an dust-enshrouded accreting stellar object line variability in integrated line flux density and line shape is expected.

v) Contributions from accretion: However, there can also be a contribution from the gas accretion of the circumstellar envelope onto the stellar surface if the DSO is a young stellar object as has already been proposed and discussed (Murray-Clay & Loeb 2012; Eckart et al. 2013; Scoville & Burkert 2013; Zajaček et al. 2014; De Colle et al. 2014). In this framework an increase of the Br γ line width as a function of time could result from an increased perturbation of the envelope or disk that leads to an enhanced velocity dispersion in the accretion stream onto the central star as it gets closer to the peribothron.

In the following we investigate if the infalling gas that is approximately in free-fall and is being shocked upon reaching the stellar surface can explain the observed large linewidth of the DSO Br γ line, that evolved from FWHM(Br γ) \sim 200 km s $^{-1}$ in 2006 to FWHM(Br γ) \sim 700 km s $^{-1}$ in 2014 as laid out in section 3.1.1 (see also, Phifer et al. 2013; Gillessen et al. 2013b). This corresponds to radial velocities v_r of infalling material that range from about 100 km s $^{-1}$ to several hundred km s $^{-1}$.

4.5.1. The model geometry

For simplicity, we consider an *axisymmetric magnetospheric accretion model* (see Bouvier et al. 2007, for review) for the accretion on pre-main sequence stars where the gas moves ballistically along the magnetic field lines from the innermost orbit of the disk and gains large infall velocities of the order of \sim 100 km s $^{-1}$ (Hartmann et al. 1994). Unlike the boundary layer model, the magnetospheric accretion scenario can indeed explain observed redshifted absorption minima at free-fall velocity and blue-ward asymmetry in emission lines (Muzerolle et al. 1998a, and references therein).

The presence of a magnetic field around pre-main sequence stars is justified by the observation of the Zeeman broadening of photospheric lines (Johns-Krull et al. 1999, 2001) as well as by

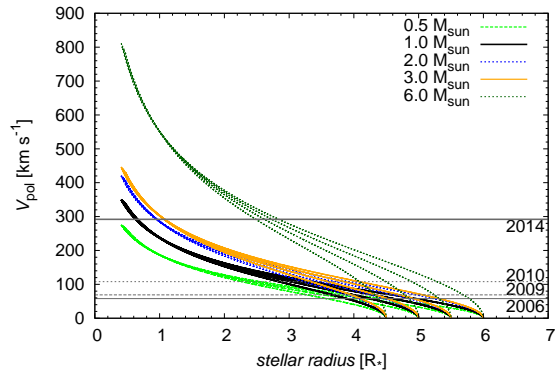


Fig. 12.— The poloidal velocity profile as a function of the distance from the pre-main sequence star in a magnetospheric accretion model (Hartmann et al. 1994) for different masses of pre-main sequence stars at \sim 1 Myr (Siess et al. 2000). The gray horizontal lines represent the observed radial velocity for years 2006, 2009, 2010, and 2014 with an increasing tendency (Phifer et al. 2013; Gillessen et al. 2013b, this work).

the measurement of the electron cyclotron maser emission (Smith et al. 2003). The inferred field strength is \sim 1–3 kG. In the context of the dipole magneto-accretion model, in which the gas is in free-fall, the truncation radius in terms of stellar radii is (e.g., Bouvier et al. 2007):

$$\frac{R_T}{R_*} \approx 6.5 B_3^{4/7} R_2^{5/7} \dot{M}_{-8}^{-2/7} M_1^{-1/7}, \quad (1)$$

where the strength of the dipole magnetic field at the equator B_3 is in kG, the stellar radius R_2 is in units of $2R_\odot$, the accretion rate \dot{M}_{-8} is expressed in $10^{-8} M_\odot \text{yr}^{-1}$, and the stellar mass M_1 is in units of $1M_\odot$. The truncation radius in Eq. 1 is derived for gas in free-fall in the spherical symmetry. For disk accretion it may serve as an upper limit, since the ram gas pressure is higher in that case and the truncation radius is thus shifted inwards.

For stable accretion to proceed, the truncation radius expressed by Eq. 1 has to be smaller than the corotation radius R_{co} , $R_T \lesssim R_{co}$, at which the Keplerian angular velocity is equal to the rotational angular velocity of the star,

$$R_{co} \approx 4.2 M_1^{1/3} P_1^{2/3} R_\odot, \quad (2)$$

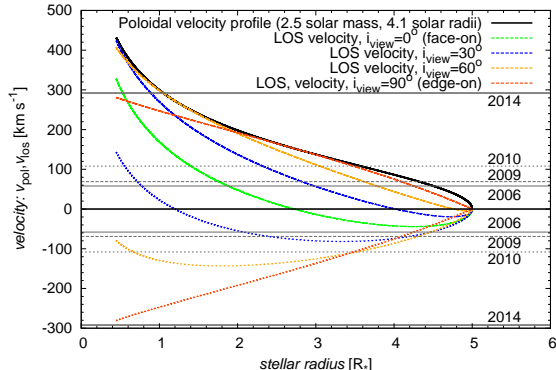


Fig. 13.— The profiles of maximum line-of-sight velocity as a function of the distance from the star in a magnetospheric accretion model (Hartmann et al. 1994) for $2.5 M_{\odot}$ pre-main sequence star for a different inclination of the view of emerging radiation. The receding flow (nearer to the observer, mostly red-shifted, positive velocities) is labeled by dashes, the approaching flow (further away, mostly blue-shifted, negative velocities) is represented by dots. The gray horizontal lines represent the observed radial velocity $v \sin i$ for years 2006, 2009, 2010, and 2014 with an increasing tendency (Phifer et al. 2013; Gillessen et al. 2013b, this work).

where M_1 is the stellar mass in units of $1 M_{\odot}$ and P_1 is the stellar rotation period in units of 1 day (see Bouvier et al. 2007, for discussion). The inner portion of the disk is purely made up of gas up to the dust sublimation radius, which according to simulations by Whitney et al. (2004), may be expressed in terms of the dust sublimation temperature and the stellar effective temperature as,

$$R_{\text{sub}} = R_{\star} \left(\frac{T_{\text{sub}}}{T_{\star}} \right)^{-2.085}, \quad (3)$$

which for typical values of T_{\star} (spectral types K, M: 3000–4500 K) and $T_{\text{sub}} \approx 1500$ K has values of ~ 4 – $10 R_{\star}$. Beyond the dust sublimation radius dust can coexist with the gaseous phase. The emerging radiation from the accretion flow is reprocessed by the circumstellar dust, giving rise to the infrared excess.

For the calculation of the velocity profiles of the accretion flow we assume the truncation radius to be at $R_{\text{T}} = 5 R_{\star}$ (Gullbring et al. 1998;

Alcalá et al. 2014), which is close to the estimate in Eq. 1. We compute the poloidal velocity profiles in the framework of the magnetospheric accretion model (see Eq.1 and 3 of Hartmann et al. 1994) for 0.5, 1.0, 2.0, and 3.0 M_{\odot} pre-main sequence stars with a stellar radius of 2.1, 2.6, 3.6, and 4.8 R_{\odot} , respectively, at 1 Myr (Siess et al. 2000) for solar metallicity and no overshooting. See Fig. 12 for the comparison of the poloidal velocity for the observed radial velocity, which is observed to increase with the approach of the DSO to the peribothron. For earlier epochs the observed FWHM is consistent with the accretion onto a low-mass object of ~ 0.5 – $1 M_{\odot}$. To explain the higher FWHM in 2014 a massive pre-main sequence star of Herbig Ae/Be type is needed at the first glance, since for lower-mass stars only the upstream parts reach comparable velocities. See the poloidal velocity profile of $6 M_{\odot}$ star with the radius of $2.9 R_{\odot}$ in Fig. 12. However, such a massive stellar core having a luminosity of $\gtrsim 100 L_{\odot}$ is inconsistent with the luminosity constraint on the DSO ($\leq 10 L_{\odot}$) and the pre-main sequence stage is also very short (Siess et al. 2000).

The physics of circumstellar material of pre-main sequence stars is generally more complex, especially close to the SMBH, where the disk surrounding the star is expected to be warped and perturbed by tidal effects. Although basic observational signatures of pre-main sequence stars (strong stellar magnetic fields, truncation radius, accretion shocks observed mainly for classical pre-main sequence stars) are in accordance with the magnetospheric accretion model (Bouvier et al. 2007) and suggest that Br γ originates in gas infall rather than outflow (Najita et al. 1996), it is plausible that there is a contribution to Br γ emission from stellar or disk winds

We note that the line profile may be generally non-symmetric and its width dependent on the inclination, at which the emerging emission is viewed. This is demonstrated by the profiles of the maximum line-of-sight velocity in Fig. 13, where we plot separately approaching (mostly blue-shifted) and receding (mostly red-shifted) accretion streams for $2.5 M_{\odot}$ pre-main sequence stars (at ~ 1 Myr, Siess et al. 2000). The separation between the dashed and the dotted lines for each stellar radius and inclination is an approximate measure of the observed linewidth.

The line broadening is generally bigger for a larger inclination (see also Muzerolle et al. 1998a, for detailed radiative transfer modeling). The results in Fig. 13 clearly show that with a star of about $2 M_{\odot}$ the observed Br γ line widths, covering the full range from about 200 km s^{-1} to 700 km s^{-1} can be reproduced. From the range of maximum and minimum velocities it is also evident that the line profile can be asymmetric and skewed to one side.

4.5.2. Accretion luminosity and rate

In fact, the broad hydrogen Br γ line with the full width at half maximum of the order of $\sim 100 \text{ km s}^{-1}$ is frequently observed in the spectra of accreting pre-main sequence stars (detection rate 70%–74%, Folha & Emerson 2001; Ilee et al. 2014) and appears to be a useful tracer of magnetospheric accretion on embedded pre-main sequence stars (Muzerolle et al. 1998b,a; Folha & Emerson 2001; Calvet et al. 2004). Here the star is assumed to accrete matter from its envelope or the inner edge of an accretion disk. Accretion from the surrounding interstellar medium can be considered as insignificant.

The correlation between Br γ emission-line luminosity and accretion luminosity is found to be tight (Muzerolle et al. 1998b; Calvet et al. 2004). The empirical relation between emission line and accretion luminosities is based on various signatures of accretion luminosity (H α luminosity, optical and UV excess). The recent fit is as follows (Alcalá et al. 2014),

$$\log(L_{\text{acc}}/L_{\odot}) = \zeta_1 \log[L(\text{Br}\gamma)/L_{\odot}] + \zeta_2. \quad (4)$$

with $\zeta_1 = 1.16 \pm 0.07$ and $\zeta_2 = 3.60 \pm 0.38$. This correlation may then be extended to heavily extincted proto-stars that are enshrouded in a dusty envelope.

If we naively apply this relation to the DSO and its Br γ emission-line luminosity of $L(\text{Br}\gamma) = f_{\text{acc}} \times 10^{-3} L_{\odot}$, where f_{acc} is a factor of the order of unity, we get a reasonable range for the accretion luminosity, $\log(L_{\text{acc}}/L_{\odot}) \approx 1.16 \log f_{\text{acc}} + 0.12$; $L_{\text{acc}} = 1.3 \times 14.5^{\log f_{\text{acc}}} L_{\odot}$, and for $f_{\text{acc}} = \{1, 2, 3, 4\}$ yielding $\{1.3, 3.0, 4.7, 6.6\} L_{\odot}$.

For the assumption of the innermost radius of $R_{\text{in}} = 5 R_{\star}$, the accretion rate is given by

(Gullbring et al. 1998)

$$\dot{M}_{\text{acc}} \cong \frac{L_{\text{acc}} R_{\star}}{GM_{\star}} \left(1 - \frac{R_{\star}}{R_{\text{T}}}\right)^{-1} \quad (5)$$

which can be written as

$$\dot{M}_{\text{acc}} \approx \xi \left(\frac{L_{\text{acc}}}{L_{\odot}}\right) \left(\frac{R_{\star}}{R_{\odot}}\right) \left(\frac{M_{\star}}{M_{\odot}}\right)^{-1} M_{\odot} \text{yr}^{-1} \quad (6)$$

with $\xi = 4.1 \times 10^{-8}$.

Inserting the estimated values for mass, radius, and the accretion luminosity, we obtain an accretion rate of the order of $\lesssim 10^{-7} M_{\odot} \text{yr}^{-1}$, which is about ten times larger than the median value observed for pre-main sequence stars in Taurus and Chameleon I regions (Hartmann et al. 1998). It is, however, consistent with the span of pre-main sequence accretion rates, which seem to evolve with the age of the pre-main sequence star as $\dot{M}_{\text{acc}} \propto t^{-2.1}$ (Baxter et al. 2008).

The gas outflow rate was shown to correlate with the accretion in pre-main sequence systems. The ratio of rates was established approximately as $\dot{M}_{\text{w}}/\dot{M}_{\text{acc}} \sim 0.1$ (Edwards et al. 2006, and references therein), which corresponds to the order of $\dot{M}_{\text{w}} \lesssim 10^{-8} M_{\odot} \text{yr}^{-1}$. This order of magnitude for the wind outflow rate was discussed by Scoville & Burkert (2013) for the wind-wind bow-shock origin of Br γ emission.

The estimates of accretion luminosity and accretion and mass-loss rates are upper limits since there may be contribution to Br γ flux from other sources than accretion flows, namely stellar wind or disk outflows (Kraus et al. 2008).

4.5.3. Density and emission measure

The radial density profile of the accretion flow may be inferred based on the estimated values of pre-main sequence star mass, radius, mass accretion rate and the assumed size of the magnetosphere. Assuming an axisymmetric steady flow of matter along the streamlines, the following relation holds for the hydrogen number density (Hartmann et al. 1994),

$$n_{\text{H}}(r) = \frac{\dot{M}_{\text{acc}}}{4\pi m_{\text{H}} \left(\frac{1}{r_{\text{mi}}} - \frac{1}{r_{\text{mo}}}\right)} \frac{r^{-5/2}}{(2GM_{\star})^{1/2}} \frac{(4-3y)^{1/2}}{(1-y)^{1/2}}, \quad (7)$$

where the magnetic streamlines are described by $r = r_m \sin^2 \theta$, where θ denotes the angle between the magnetic dipole axis and the radius-vector \mathbf{r} ; in Eq. 7 $y = r/r_m = \sin^2 \theta$ and r_{mi} and r_{mo} stand for the radius of the innermost and the outermost streamline intersecting the accretion disk, respectively; we take $r_{mi} = 5 R_\star$ and $r_{mo} = 7 R_\star$ for definiteness. The mass accretion rate is held fixed at $\dot{M}_{acc} = 10^{-7} M_\odot \text{yr}^{-1}$ in accordance with Eq. 6. The density profiles for the same set of stars as in Fig. 12 are plotted in Fig. 14.

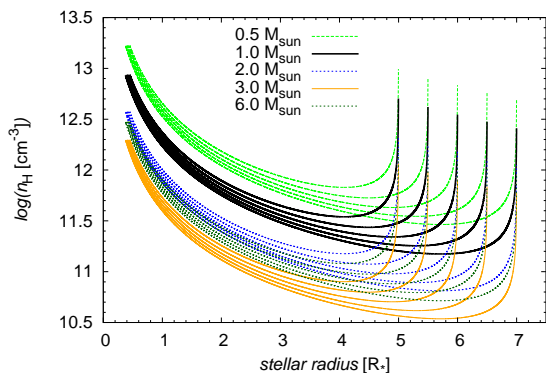


Fig. 14.— The radial number density profile as a function of the distance from the star in units of stellar radii. The computed profile is valid for the steady axisymmetric accretion on a pre-main sequence star. Individual lines correspond to accretion flows along magnetic streamlines for a particular mass of a star (see the labels). The radius of a star is adopted from the evolutionary tracks of Siess et al. (2000) at ~ 1 Myr.

The density profile in Fig. 14 enables to estimate the emission measure, $EM \propto n_e^2 V$, under the assumption $n_e \approx n_H$, see Eq. 7. The computation is performed for the distance range where the poloidal velocity, Fig. 12, reaches the values of $v_{pol} = 200 \pm 100 \text{ km s}^{-1}$, which roughly corresponds to the observed FWHM of the Br γ line. Finally, we get the profiles of cumulative emission measure for a different mass of a pre-main sequence star according to the evolutionary tracks by Siess et al. (2000) at ~ 1 Myr, see Fig. 15. The emission measure is of the order of $10^{58} - 10^{61} \text{ cm}^{-3}$, being higher for lower-mass stars, and these values originate from close to the star, on

the scale of $\sim 1-3 R_\star$. This implies that luminous line emission at the observed high velocities can originate from close to a few solar mass star.

One should consider these values highly estimative because of the uncertain values of mass-accretion rate and the size and character of the magnetosphere. The temperature of the accretion flow was also not discussed. However, models of the accretion on pre-main sequence stars show that the infalling gas is shock-heated and the Br γ line can be effectively produced close to the stellar surface (Bouvier et al. 2007). In principle it is possible to reproduce the emission measure of $\sim 10^{57} \text{ cm}^{-3}$ that is obtained in the cold bow-shock model by Scoville & Burkert (2013) and that corresponds to the observed flux of Br γ emission. Thus both mechanisms, wind-wind interaction and gas infall, can contribute in case the DSO is a young stellar object.

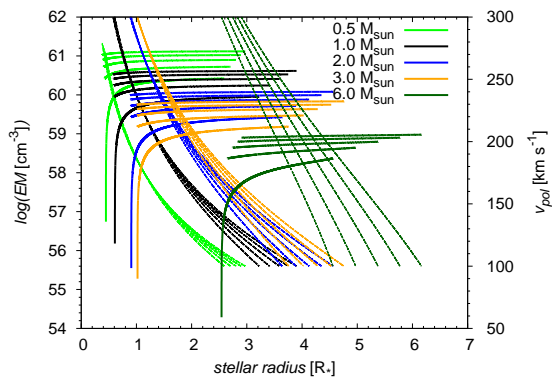


Fig. 15.— The logarithm of emission measure EM (solid lines, with labels on the left vertical axis) and poloidal velocity profile v_{pol} (dot-dashed lines, with labels on the right vertical axis) as a function of the distance from the star in units of stellar radii. The computed profile is valid for the steady axisymmetric accretion on a pre-main sequence star. Individual lines correspond to accretion flows along magnetic streamlines for a particular mass of a star (see the key). The radius of a star is adopted from the evolutionary tracks of Siess et al. (2000) at ~ 1 Myr.

Given the accretion rate of $\lesssim 10^{-7} M_\odot \text{yr}^{-1}$ the star associated with the DSO would be embedded within the hot accretion flow surrounding the star with a probably complex geometry. On

the length-scale of one stellar radius the density profiles in Fig. 10 imply large infrared K-band and visible extinction of $A(K) \sim 0.1 \times A(V) \approx 0.1 \times (1.8 \times 10^{21})^{-1} \int n_e(l) dl$, which is $\sim 59, 37, 20$, and 16 magnitudes for a $0.5 M_\odot, 1.0 M_\odot, 2.0 M_\odot$, and $3.0 M_\odot$ star, respectively. Combined with the possible contribution of an extended outer dust shell and a warped or inflated outer disk, this is plenty of extinction to dim the light from the central star and produce the observed continuum characteristics of the DSO (Eckart et al. 2014a,b, 2013; Phifer et al. 2013; Gillessen et al. 2012),

The material within the accretion flow is certainly not homogeneous. To first order we assume that it consists of cloudlets, sheets or filaments that have a dense, optically thick core surrounded by a shell of optically thin material. Since the overall line emission is dominated by optically thin material and given the uncertainties in the $\text{Pa}\alpha/\text{Br}\gamma$ and $\text{He I}/\text{Br}\gamma$ line ratios the maximum contribution of the optically thick material to the line fluxes can only be of the order of 0.05. Since the dense material is bright the ratio η between the mean emission measure of the optically thin and thick material needs to be involved. Hence a volume filling factor around $0.05 \times \eta$ will reproduce the optically thin line ratios and give a substantial contribution to the observed velocity profile. In addition, there will be a temperature gradient from the start of the accretion stream near the dust sublimation radius and the contact point on the stellar surface, leading to an enhanced contribution of the higher velocity material.

The observed accreting pre-main sequence stars generally have a lower accretion rate than the time-averaged infall rate (Audard et al. 2014). As a result, the gas from an infalling envelope is thought to be accumulated first in the quasi-Keplerian circumstellar disk. The accumulation of matter continues until the instability causes an increase in the mass transfer by about three–four orders of magnitude from the disk to the star, the so-called episodic accretion (Audard et al. 2014). If the DSO is indeed an embedded accreting pre-main sequence star, the tidal effects from the SMBH lead to a gravitational instability which, combined with magneto-rotational instability (Zhu et al. 2009), can cause a continual mass transfer from the disk, especially close to the peribothron where the tidal radius shrinks to

$\lesssim 1 \text{ AU}$ for a $1 M_\odot$ star, see also the tidal radius discussion related to Fig. 16.

Let us sum up that the observed emission up to now is not in contradiction with the scenario of a pre-main sequence star that is surrounded by a dusty envelope and accretes matter from an accretion disk inside the dust sublimation radius. Hot accretion flows as discussed here, possibly combined with disk winds (Günther 2011), can indeed produce emission lines with FWHM of several hundred km/s. Hence we find that for a 1-2 M_\odot embedded pre-main sequence star these two effects can already fully account for the observed $\text{Br}\gamma$ line widths. However, in general the observed $\text{Br}\gamma$ line profile and flux may result from the combination of hydrogen recombination emission of the gaseous-dusty envelope photoionized by nearby stars (Shcherbakov 2014), collisionally ionized cold bow-shock layer (Scoville & Burkert 2013), and the hot accretion flow on a pre-main sequence star, as is discussed here. If and to what extent each of these processes contributes to the final emission will be constrained by further observations and modeling during the post-peribothron phase.

5. Possible origin, stability and fate of the DSO

There is evidence of both young and more evolved stars in the Galactic centre (Genzel et al. 2010) that lie in the sphere of influence ($\sim 2 \text{ pc}$) of the super massive black hole (SMBH). Mutual interactions among stars cause the oscillations of their orbital eccentricity via the mechanism of resonant relaxation (Hopman & Alexander 2006) or the Kozai oscillations (Karas & Šubr 2007; Chen & Amaro-Seoane 2014). These can set some stars on a plunging trajectory towards the SMBH (Zajaček et al. 2014). Similarly, with Jalali et al. (2014) we have shown that young stellar objects can efficiently be formed on plunging orbits in the vicinity of super massive black holes as a consequence of orbital compressing of infalling gas clumps. An embedded young star/protostar is surrounded by an accretion disk whose orbit orientation can be any (direct, retrograde or perpendicular) with respect to the orbit of the host star around the SMBH. These dusty S-cluster objects (DSOs; Eckart et al. 2013) have an infrared excess

and the currently observed DSO may indeed serve as a paradigm of these objects.

The restricted three-body problem may be used to obtain the approximations for critical stability (Hill) radii of disks. Using the restricted circular three-body problem the equation of motion for a mass element in the rotating frame of star-SMBH becomes (i.e., Innanen 1979, 1980):

$$\frac{d^2r}{dt^2} \simeq \left(\Omega^2 - \frac{d^2V}{dR^2} - \frac{GM_\star}{r^3} \right) r \pm 2\Omega v_r, \quad (8)$$

where r is the distance of a mass element from the star and R labels the distance of the star from the SMBH, $r \ll R$. For $R \gg R_g$, the gravitational potential of the black hole is approximately equal to the Newtonian $V \equiv V(R)$, hence $-d^2V/dR^2 = 2GM_\bullet/R^3$. The angular frequency of the circular motion for the star is $\Omega^2 = GM_\bullet/R^3$ and for the minor body $\omega^2 = GM_\star/r^3$. The difference between direct and retrograde orbits arises from the different signs of the Coriolis term $\pm 2\Omega v_r$, where $v_r = \omega r$.

When generalized for orbits with eccentricity e , one gets the following ratio of critical tidal radii for retrograde and direct disks, $r_{H,r}$ and $r_{H,d}$, respectively (Innanen 1979):

$$\frac{r_{H,r}}{r_{H,d}} = \left[\frac{5 + e + 2(4 + e)^{1/2}}{3 + e} \right]^{2/3}, \quad (9)$$

In terms of the critical tidal radius,

$$r_t = R(t)(M_\star/(3M_\bullet))^{1/3}, \quad (10)$$

the critical Hill radius for prograde orbits r_d and retrograde orbits r_r may be expressed as $r_r = 3^{1/3}r_t$ and $r_d = 3^{-1/3}r_t$. Since the mass of the SMBH M_\bullet is larger by at least 5 orders of magnitude than the mass of any star M_\star , the tidal Hill radius r_t expressed by eq. 10 extends up to Lagrangian points L1 and L2, beyond which the circumstellar matter is strongly tidally perturbed and may escape the Roche lobe of the star (see Fig.18 by Eckart et al. 2013). The temporal evolution of the tidal radii for the current orbital elements and the stellar mass of $m_\star = 1 M_\odot$ is shown in Fig. 16.

The ratio $r_{H,r}/r_{H,d}$ acquires values of (1.9, 2.1) for eccentricities $e \in (1, 0)$. Therefore retrograde

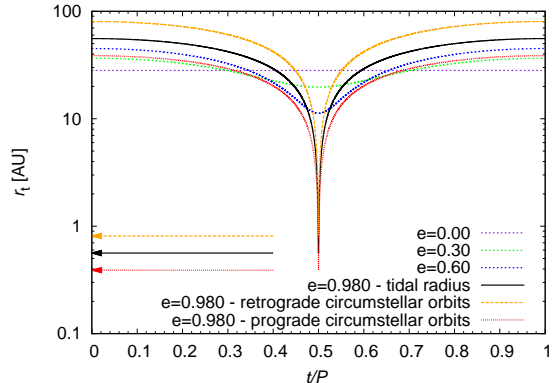


Fig. 16.— Temporal evolution of the tidal Hill radius for the orbits of a $1M_\odot$ star around the SMBH with a different orbital eccentricity. At $t/P = 0.5$ the pericenter passage occurs. For the inferred orbit of the DSO, tidal radii for prograde as well as retrograde orbits are depicted. Actual values of the tidal radii at the peribothron are depicted by corresponding arrows. The current orbital solution implies a considerable tidal stripping for distances from the star $\gtrsim 1$ AU.

orbits are expected to be stable for larger distances from the host star, approximately by the factor of two for low-inclination orbits. See Fig. 17 for the polar plot of the dependence of the ratio of tidal Hill stability radii $r_{H,r}/r_{H,d}$ on the inclination i_D between a putative circumstellar accretion disk and the orbital plane of DSO.

6. Conclusions

In our sensitive imaging spectroscopy data set we measured prominent line emission from the DSO, and determined new orbital parameters based on data from February till September 2014. The source appeared to be single lined at all times. Before the peribothron we detected red-shifted Br γ line emission (at 2700 km/s) but no blue-shifted emission above the noise level at the position of SgrA* or upstream the presumed orbit. After the peribothron we detected blue-shifted Br γ line emission (at -3320 km/s) but no red-shifted emission above the noise level at the position of SgrA* or downstream the presumed orbit. We find a Br γ -line full width at half maximum of $50 \pm 10 \text{ \AA}$ before and $15 \pm 10 \text{ \AA}$ after the peribothron transit, i.e. no significant line broad-

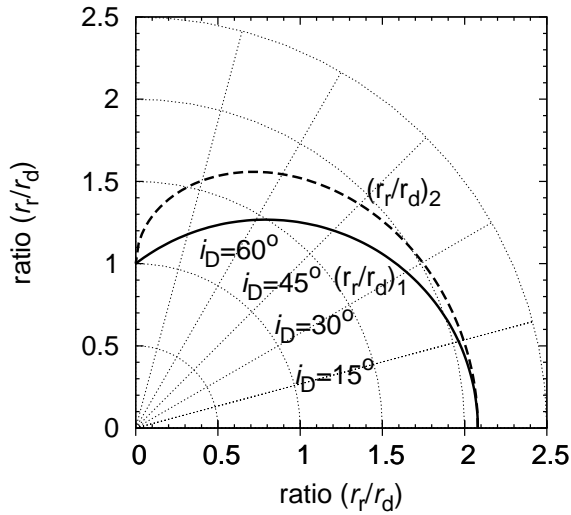


Fig. 17.— The polar plot of the dependence of the ratio of critical tidal radii of retrograde (r_r) and prograde (r_d) disks on the inclination of the accretion disk around a pre-main sequence star with respect to the orbital plane of the star around the SMBH. In this plot the vertical and horizontal axis represent the same quantity - the ratio between retrograde and prograde tidal radii. The ratio dependence on the inclination was derived by Innanen (1980). The plotted relations have the form of $(r_r/r_d)_{1,2} = \{1 + f_{1,2}/2 + [f_{1,2} + (f_{1,2}/2)^2]^{1/2}\}^{2/3}$, where $f_1 = 4(\cos^2 i)/3$ and $f_2 = 4 \cos i/(2 + \cos i)$. The relation $(r_r/r_d)_1$ dominates the second one. The largest difference between the critical tidal radii of a factor of ~ 2 is for low-inclination orbits with respect to the orbital plane of DSO.

ening with respect to last year is observed. Such a broadening would be expected in case of significant tidal interaction. This is a further indication for the fact that the DSO is spatially rather compact.

We show that for a 1 - 2 M_\odot embedded pre-main sequence star hot accretion streams close to the star possibly in combination with disk winds can fully account for the luminous observed Br γ emission with line widths covering the full range from about 200 km s^{-1} to 700 km s^{-1} . The accretion material and the surrounding shell/disk provide enough extinction to explain the infrared colors of the DSO (Eckart et al. 2013). The re-

sulting line profile can be asymmetric and skewed to one side calling for precaution when using the line emission to derive orbital parameters. Following the pre-main sequence evolutionary tracks of low- and intermediate-mass stars by Siess et al. (2000) we find that after an initial phase of a few 10^5 years 1-2 M_\odot stars can stay for a major portion of their T Tauri stage with a luminosity of less than 10 L_\odot (see also Chen & Amaro-Seoane 2014). This is consistent with a dust temperature of 450 K and a possible spectral decomposition of the NIR/MIR spectrum (Eckart et al. 2013) of the DSO using the M-band measurement by Gillessen et al. (2012). Higher stellar masses would not comply with this luminosity limit and are not required to explain the Br γ line widths. An embedded pre-main sequence star can also explain the increase of the Br γ line width assuming that tidal stretching and perturbation of the envelope lead to an enhancement of the velocity dispersion in the accretion stream onto the central star as the DSO approaches the peribothron. An identification of the DSO with a dust embedded star also puts the interpretation of a common history of the DSO/G2 and G1 at risk (Pfuhl et al. 2014). Due to the higher mass (1-2 M_\odot instead of 3 earth masses) a very much higher drag force than the one provided by the small source size would be required to connect the DSO orbit to that of G1.

We also find that the NIR flaring activity of SgrA* has not shown any statistically significant increment. This points at the fact that the DSO had not yet reached its peribothron before May 2014. Even if the source has a stellar core a major part of the enshrouding cloud may be dissolved during the peribothron passage. Therefore increased accretion activity of SgrA* may still be upcoming. The SgrA*/DSO system can be looked upon as a binary system and the Roche lobe picture can be adopted in which the Lagrange point L1 between the two objects is of special importance if mass transfer between the two objects needs to be considered. If the central star has around one solar mass the L1 will get very close (~ 1 AU) and may allow the dominant part of the gas and dust to transit into the SgrA* dominated Roche lobe. As a result the low mass stellar core may be even less luminous after the transit than the matter in its immediate vicinity (i.e. 1 AU) before the transit. This will, however, be only for

a very short time and it is not clear if the gas close to the star will remain in the Roche lobe of the star after peribothron or not. For higher mass stellar cores that were heavily extinguished before peribothron most of the material closer to the stars (i.e. a few AU) may be largely unaffected by the transition and the stellar core may be even cleared from extinguishing material and brighter in the NIR-bands than before the peribothron .

In the near future it will become increasingly difficult to measure the strength and spatial extent of the line emission on the blue side of the orbit. This is due to a high velocity star that is moving into this field from the northwest. It will then be followed by S2 going through peribothron around 2017.9 ± 0.35 (Gillessen et al. 2009; Eisenhauer et al. 2003) and S0-102 around 2021.0 ± 0.3 (Meyer et al. 2014a,b). Strong continuum contributions and residual line features in the stellar atmospheres may make sensitive observations very difficult and time consuming.

The research leading to these results received funding from the European Union Seventh Framework Program (FP7/2007-2013) under grant agreement n312789. This work has been financially supported by the Programme National Hautes Energies (PNHE). This work was supported in part by the Deutsche Forschungsgemeinschaft (DFG) via the Cologne Bonn Graduate School (BCGS), the Max Planck Society through the International Max Planck Research School (IMPRS) for Astronomy and Astrophysics, as well as special funds through the University of Cologne. M. Zajacek, B. Shahzamanian, S. Smajic, A. Borkar are members of the IMPRS. Part of this work was supported by fruitful discussions with members of the European Union funded COST Action MP0905: Black Holes in a violent Universe and the Czech Science Foundation – DFG collaboration (No. 13-00070J). This work was co-funded under the Marie Curie Actions of the European Commission (FP7-COFUND). Macarena García-Marín is supported by the German federal department for education and research (BMBF) under the project number 50OS1101. We are grateful to all members of the ESO PARANAL team.

REFERENCES

Alcalá, J. M., Natta, A., Manara, C. F., et al.

- 2014, *A&A*, 561, A2
- Audard, M., Ábrahám, P., Dunham, M. M., et al. 2014, ArXiv e-prints, arXiv:1401.3368
- Baganoff, F. K., Bautz, M. W., Brandt, W. N., et al. 2001, *Nature*, 413, 45
- Baganoff, F. K., Maeda, Y., Morris, M., et al. 2003, *ApJ*, 591, 891
- Ballone, A., Schartmann, M., Burkert, A., et al. 2013, *ApJ*, 776, 13
- Barrière, N. M., Tomsick, J. A., Baganoff, F. K., et al. 2014, *ApJ*, 786, 46
- Baxter, E., Corrales, L., Yamada, R., & Esin, A. A. 2008, *ApJ*, 689, 308
- Bonnet, H., Abuter, R., Baker, A., et al. 2004, *The Messenger*, 117, 17
- Bouvier, J., Alencar, S. H. P., Harries, T. J., Johns-Krull, C. M., & Romanova, M. M. 2007, *Protostars and Planets V*, 479
- Burkert, A., Schartmann, M., Alig, C., et al. 2012, *ApJ*, 750, 58
- Calvet, N., Muzerolle, J., Briceño, C., et al. 2004, *AJ*, 128, 1294
- Cantó, J., Raga, A. C., & González, R. 2005, *Rev. Mexicana Astron. Astrofis.*, 41, 101
- Capelli, R., Warwick, R. S., Porquet, D., Gillessen, S., & Predehl, P. 2012, *A&A*, 545, A35
- Chen, X., & Amaro-Seoane, P. 2014, *ApJ*, 786, L14
- Crumley, P., & Kumar, P. 2013, *MNRAS*, 436, 1955
- Czerny, B., Kunneriath, D., Karas, V., & Das, T. K. 2013, *A&A*, 555, A97
- Davis, C. J., Cervantes, B., Nisini, B., et al. 2011, *A&A*, 528, A3
- De Colle, F., Raga, A. C., Contreras-Torres, F. F., & Toledo-Roy, J. C. 2014, *ApJ*, 789, L33
- Degenaar, N., Miller, J. M., Kennea, J., et al. 2013, *ApJ*, 769, 155

- Diolaiti, E., Bendinelli, O., Bonaccini, D., et al. 2000, *A&AS*, 147, 335
- Eckart, A., & Duhoux, P. R. M. 1991, in *Astronomical Society of the Pacific Conference Series*, Vol. 14, *Astronomical Society of the Pacific Conference Series*, ed. R. Elston, 336–338
- Eckart, A., García-Marín, M., Vogel, S. N., et al. 2012a, *A&A*, 537, A52
- Eckart, A., Britzen, S., Horrobin, M., et al. 2012b, in *Proceedings of Nuclei of Seyfert galaxies and QSOs - Central engine and conditions of star formation (Seyfert 2012)*. 6-8 November, 2012. Max-Planck-Institut für Radioastronomie (MPIfR), Bonn, Germany. Online at <http://pos.sissa.it/cgi-bin/reader/conf.cgi?confid=169>; <http://pos.sissa.it/cgi-bin/reader/conf.cgi?confid=169/A4>, id.4, 4
- Eckart, A., Mužić, K., Yazici, S., et al. 2013, *A&A*, 551, A18
- Eckart, A., Valencia-S., M., Peissker, F., et al. 2014a, *The Astronomer’s Telegram*, 6285, 1
- Eckart, A., Horrobin, M., Britzen, S., et al. 2014b, in *IAU Symposium*, Vol. 303, *IAU Symposium*, ed. L. O. Sjouwerman, C. C. Lang, & J. Ott, 269–273
- Edwards, S., Fischer, W., Hillenbrand, L., & Kwan, J. 2006, *ApJ*, 646, 319
- Edwards, S., Kwan, J., Fischer, W., et al. 2013, *ApJ*, 778, 148
- Eisenhauer, F., Abuter, R., Bickert, K., et al. 2003, in *Society of Photo-Optical Instrumentation Engineers (SPIE) Conference Series*, Vol. 4841, *Instrument Design and Performance for Optical/Infrared Ground-based Telescopes*, ed. M. Iye & A. F. M. Moorwood, 1548–1561
- Eisenhauer, F., Genzel, R., Alexander, T., et al. 2005, *ApJ*, 628, 246
- Eisner, J. A., Hillenbrand, L. A., White, R. J., et al. 2007, *ApJ*, 669, 1072
- Folha, D. F. M., & Emerson, J. P. 2001, *A&A*, 365, 90
- Genzel, R., Eisenhauer, F., & Gillessen, S. 2010, *Reviews of Modern Physics*, 82, 3121
- Ghez, A. M., Duchêne, G., Matthews, K., et al. 2003, *ApJ*, 586, L127
- Ghez, A. M., Witzel, G., Sitarski, B., et al. 2014, *The Astronomer’s Telegram*, 6110, 1
- Gillessen, S., Eisenhauer, F., Fritz, T. K., et al. 2009, *ApJ*, 707, L114
- Gillessen, S., Genzel, R., Fritz, T. K., et al. 2012, *Nature*, 481, 51
- . 2013a, *ApJ*, 763, 78
- . 2013b, *ApJ*, 774, 44
- Gullbring, E., Hartmann, L., Briceño, C., & Calvet, N. 1998, *ApJ*, 492, 323
- Günther, H. M. 2011, *Astronomische Nachrichten*, 332, 448
- Haggard, D., Baganoff, F. K., Rea, N., et al. 2014, *The Astronomer’s Telegram*, 6242, 1
- Hartmann, L., Calvet, N., Gullbring, E., & D’Alessio, P. 1998, *ApJ*, 495, 385
- Hartmann, L., Hewett, R., & Calvet, N. 1994, *ApJ*, 426, 669
- Herczeg, G. J., & Hillenbrand, L. A. 2014, *ApJ*, 786, 97
- Hopman, C., & Alexander, T. 2006, *ApJ*, 645, 1152
- Ilee, J. D., Fairlamb, J., Oudmaijer, R. D., et al. 2014, *ArXiv e-prints*, arXiv:1409.4897
- Innanen, K. A. 1979, *AJ*, 84, 960
- . 1980, *AJ*, 85, 81
- Jalali, B., Pelupessy, F. I., Eckart, A., et al. 2014, *MNRAS*, 444, 1205
- Johns-Krull, C. M., Valenti, J. A., & Koresko, C. 1999, *ApJ*, 516, 900
- Johns-Krull, C. M., Valenti, J. A., Piskunov, N. E., Saar, S. H., & Hatzes, A. P. 2001, in *Astronomical Society of the Pacific Conference Series*, Vol. 248, *Magnetic Fields Across the Hertzsprung-Russell Diagram*, ed. G. Mathys, S. K. Solanki, & D. T. Wickramasinghe, 527

- Karas, V., & Šubr, L. 2007, *A&A*, 470, 11
- Kraus, S., Hofmann, K.-H., Benisty, M., et al. 2008, *A&A*, 489, 1157
- Lima, G. H. R. A., Alencar, S. H. P., Calvet, N., Hartmann, L., & Muzerolle, J. 2010, *A&A*, 522, A104
- Markoff, S., Bower, G. C., & Falcke, H. 2007, *MNRAS*, 379, 1519
- Markoff, S., Falcke, H., Yuan, F., & Biermann, P. L. 2001, *A&A*, 379, L13
- Marrone, D. P., Moran, J. M., Zhao, J.-H., & Rao, R. 2007, *ApJ*, 654, L57
- Martins, F., Trippe, S., Paumard, T., et al. 2006, *ApJ*, 649, L103
- Meyer, L., Witzel, G., Longstaff, F. A., & Ghez, A. M. 2014a, *ApJ*, 791, 24
- Meyer, L., Ghez, A. M., Witzel, G., et al. 2014b, in *IAU Symposium*, Vol. 303, *IAU Symposium*, ed. L. O. Sjouwerman, C. C. Lang, & J. Ott, 264–268
- Mossoux, E., Grosso, N., Vincent, F. H., & Porquet, D. 2014, *ArXiv e-prints*, arXiv:1409.6452
- Moto’oka, K., & Itoh, Y. 2013, *Research in Astronomy and Astrophysics*, 13, 1189
- Murray-Clay, R. A., & Loeb, A. 2012, *Nature Communications*, 3, arXiv:1112.4822
- Mužić, K., Eckart, A., Schödel, R., et al. 2010, *A&A*, 521, A13
- Muzerolle, J., Calvet, N., & Hartmann, L. 1998a, *ApJ*, 492, 743
- Muzerolle, J., Hartmann, L., & Calvet, N. 1998b, *AJ*, 116, 2965
- Najita, J., Carr, J. S., & Tokunaga, A. T. 1996, *ApJ*, 456, 292
- Narayan, R., Özel, F., & Sironi, L. 2012, *ApJ*, 757, L20
- Neilsen, J., Nowak, M. A., Gammie, C., et al. 2013, *ApJ*, 774, 42
- Nowak, M. A., Neilsen, J., Markoff, S. B., et al. 2012, *ApJ*, 759, 95
- Pfuhl, O., Gillessen, S., Eisenhauer, F., et al. 2014, *ArXiv e-prints*, arXiv:1407.4354
- Phifer, K., Do, T., Meyer, L., et al. 2013, *ApJ*, 773, L13
- Porquet, D., Predehl, P., Aschenbach, B., et al. 2003, *A&A*, 407, L17
- Porquet, D., Grosso, N., Predehl, P., et al. 2008, *A&A*, 488, 549
- Pych, W. 2004, *PASP*, 116, 148
- Revnivtsev, M. G., Churazov, E. M., Sazonov, S. Y., et al. 2004, *A&A*, 425, L49
- Róžańska, A., Czerny, B., Kunneriath, D., et al. 2014, *ArXiv e-prints*, arXiv:1410.0397
- Sabha, N., Eckart, A., Merritt, D., et al. 2012, *A&A*, 545, A70
- Sądowski, A., Sironi, L., Abarca, D., et al. 2013, *MNRAS*, 432, 478
- Schartmann, M., Burkert, A., Alig, C., et al. 2012, *ApJ*, 755, 155
- Schödel, R., Najarro, F., Muzic, K., & Eckart, A. 2010, *A&A*, 511, A18
- Scoville, N., & Burkert, A. 2013, *ApJ*, 768, 108
- Shcherbakov, R. V. 2014, *ApJ*, 783, 31
- Shcherbakov, R. V., & Baganoff, F. K. 2010, *ApJ*, 716, 504
- Siess, L., Dufour, E., & Forestini, M. 2000, *A&A*, 358, 593
- Sjouwerman, L. O., & Chandler, C. J. 2014, in *IAU Symposium*, Vol. 303, *IAU Symposium*, ed. L. O. Sjouwerman, C. C. Lang, & J. Ott, 327–329
- Smajić, S., Moser, L., Eckart, A., et al. 2014, *A&A*, 567, A119
- Smith, K., Pestalozzi, M., Güdel, M., Conway, J., & Benz, A. O. 2003, *A&A*, 406, 957
- Sunyaev, R., & Churazov, E. 1998, *MNRAS*, 297, 1279

- Terrier, R., Ponti, G., Bélanger, G., et al. 2010, ApJ, 719, 143
- Wang, Q. D., Nowak, M. A., Markoff, S. B., et al. 2013, Science, 341, 981
- Whitney, B. A., Indebetouw, R., Bjorkman, J. E., & Wood, K. 2004, ApJ, 617, 1177
- Wilkin, F. P. 1996, ApJ, 459, L31
- Witzel, G., Eckart, A., Bremer, M., et al. 2012, ApJS, 203, 18
- Witzel, G., Ghez, A. M., Morris, M. R., et al. 2014, ArXiv e-prints, arXiv:1410.1884
- Wolk, S. J., & Walter, F. M. 1996, AJ, 111, 2066
- Zajaček, M., Karas, V., & Eckart, A. 2014, A&A, 565, A17
- Zhu, Z., Hartmann, L., & Gammie, C. 2009, ApJ, 694, 1045